Material characterisation of additively manufactured elastomers at different strain rates and build orientations

Fady F. Abayazid, Mazdak Ghajari*

Dyson School of Design Engineering, Imperial College London, London, UK

Highlights:

- *Comprehensive mechanical tests are carried out on two new PolyJet elastomers.*
- *The stress-strain response of PolyJet elastomers is highly sensitive to strain rate.*
- *A visco-hyperelastic material model captures the strain rate sensitivity of the elastomers.*
- *The elastomers fully recover after 20 seconds after repeated cyclic loading.*
- *Anisotropy in the elastomers is dependent on strain and strain rate.*

Abstract

Material jetting, particularly PolyJet technology, is an additive manufacturing (AM) process which has introduced novel flexible elastomers used in bio-inspired soft robots, compliant structures and dampers. Finite Element Analysis (FEA) is a key tool for the development of such applications, which requires comprehensive material characterisation utilising advanced material models. However, in contrast to conventional rubbers, PolyJet elastomers have been less explored leading to a few material models with various limitations in fidelity. Therefore, one aim of this study was to characterise the mechanical response of the latest PolyJet elastomers, Agilus30 (A30) and Tango+ (T+), under large strain tension-compression and time-dependent high-frequency/relaxation loadings. Another aim was to calibrate a visco-hyperelastic material model to accurately predict these responses. Tensile, compressive, cyclic, dynamic mechanical analysis (DMA) and stress relaxation tests were carried out on pristine A30 and T+ samples. Quasi-static tension-compression tests were used to calibrate a 3-term Ogden hyperelastic model. Stress relaxation and DMA results were combined to determine the constants of a 5-term Prony series across a large window of relaxation time (10 µs - 100 s). A numerical time-stepping scheme was employed to predict the visco-hyperelastic response of the 3D-printed elastomers at large strains and different strain rates. In addition, the anisotropy in the elastomers, which stemmed from build orientation, was explored. Highly nonlinear stress-strain relationships were observed in both elastomers, with a strong dependency on strain rate. Relaxation tests revealed that A30 and T+ elastomers relax to 50% and 70% of their peak stress values respectively in less than 20 seconds. The effect of orientation on the loading response was most pronounced with prints along the Z-direction, particularly at large strains and lower strain rates. Moreover, the visco-hyperelastic material model accurately predicted the large strain and time-dependent behaviour of both elastomers. Our findings will allow for the development of more accurate computational models of 3D-printed elastomers, which can be utilised for computer-aided design in novel applications requiring flexible or rate-sensitive AM materials.

Keywords: Material jetting; PolyJet elastomers; visco-hyperelastic rubbers; material characterisation; anisotropy

Introduction

Additive manufacturing (AM), commonly known as 3D-printing, has rapidly closed the gap between product design, prototyping and final production. Commercial parts with often critical contribution to functionality are now produced via AM such as automotive brake callipers [1], aerospace parts [2], customised medical and prosthetic implants [3–6] and energy absorbing lattice structures [7–11].

One of the most promising AM methods is photopolymer jetting (PolyJet), also known as material jetting. PolyJet involves the deposition of voxel-based droplets of photopolymer resins onto a print bed, after which the resins are cured using ultraviolet (UV) lamps [12,13]. This method polymerises the deposited layer and allows for another layer to be added. The layer-by-layer nature of PolyJet makes it one of the fastest AM technologies that currently exist in contrast to line-by-line AM processes such as fused deposition modelling (FDM) or powder-bed fusion (PBF) [13]. Moreover, the deposition of the resin prior to curing means that a wide range of resins with different polymerised properties, called 'Digital Materials' (DMs), can be deposited from the same set of nozzles allowing for the production of multi-material parts [14–16]. In recent years, new flexible elastomers, such as Agilus30 (A30) and Tango+ (T+), have become available to PolyJet technology through the development of novel photopolymer resins. The mechanical flexibility of PolyJet elastomers have made them particularly useful for applications including soft robotic active hinges and actuators [14,17,18], shape memory '4D materials' and composites [14,19–24]. Other applications included wearable electronics [25], compliant systems and metamaterials [15,26].

Computational modelling methods, particularly Finite Element Analysis (FEA), have played a key role in accelerating the development of several of such complex structures that are subjected to large strains and a range of strain rates. This has provided engineers with insight into the performance of their designs in ways otherwise unobtainable. However, it is paramount that material models are well calibrated to experimental tests relevant to the strain and strain rates expected for reliable computational predictions. This is particularly important when the materials employed are viscoelastic, i.e. time-dependent and sensitive to rate of loading, such as industrial rubbers and the growing family of PolyJet elastomers such as those explored here.

The existing material models of PolyJet elastomers in the literature are widely inconsistent as their time-dependency is often oversimplified [27,28] or entirely overlooked [29–33]. A recent study collected the shear modulus of several of the existing material models for T+ and reported a variation from 0.158 - 0.330 MPa [27]. Reasons for this could be that studies regarded Tango (T) and T+ as linear elastic [33,34] or purely hyperelastic using Neo-Hookean [30] or Arruda-Boyce material models [35], disregarding their time-dependent behaviour. The majority of studies which have explored PolyJet elastomers have focused on their time-independent behaviour [14,27,36]. Ryu et al. explored the accuracy of Neo-Hookean and Mooney-Rivlin hyperelastic material models in predicting the uniaxial tensile response of TangoBlack+ (TB+) alongside other DMs using FEA [37]. Salcedo et al. explored the DM composites by assessing their tensile response with TB+ elastomer and rigid VeroWhite (VW+) co-printed within the same sample with various arrangements [38]. However, none of the studies have explored the viscoelastic response of the elastomers, which we have found to significantly alter the response of the PolyJet elastomers. This renders the existing data insufficient for extracting comprehensive material properties that can accurately represent the mechanical response of the elastomers across a range of loading speeds.

To bridge this gap, we present a comprehensive set of experimental results conducted on pristine A30 and T+ samples, including tensile, compressive, cyclic loading tests as well as dynamic

mechanical analysis (DMA) and stress relaxation tests. We then present a visco-hyperelastic material model that can accurately predict the time-dependent properties of the elastomers across two decades of strain rates. To our best knowledge, this is the first paper to provide a visco-hyperelastic material model for PolyJet elastomers using stress relaxation and uniaxial test data.

The importance of modelling viscoelasticity of materials can be seen in [17,39]. Therein, the authors reported significant relaxation of their PolyJet-printed bellow actuators which was not modelled due to insufficient data on the time-dependency and viscoelastic modelling of A30.

Here, we use our experimental data to determine the constants of a time-dependent material model for both T+ and A30 to predict the response of these PolyJet elastomers to tension and compression with promising fidelity across strain rates spanning two orders of magnitude.

Another attribute of PolyJet parts, which is common in several AM methods, is the inherent anisotropy in the final part due to the difference between the inter- and intra-layer mechanical properties [40–46]. Previous studies reported that elastic moduli, ultimate tensile strength and fracture stress of PolyJet plastics all varied with build orientation [40,42–44]. A few studies on the anisotropy of PolyJet elastomers concluded that parts printed along the print bed (X-Y) plane had the highest elastic modulus [36,47–49]. However, no studies to date have reported the effect of build orientation on the nonlinear time-dependent stress response of PolyJet elastomers. Here we also studied the effect of PolyJet build orientation on the mechanical response of T+ and A30 elastomers at various strain rates. As isotropy was assumed for the presented visco-hyperelastic material model, our work also provides insight into the fidelity of the presented material model in predicting A30 and T+ responses along different build orientations.

Methods

Experimental Methods

Connex3 Objet500 and Objet260 multi-material 3D-printers were used to print clear A30 and T+ samples respectively (Connex3, Stratasys ltd.). All samples were printed in a single print job as per the arrangement in Figure 1 with one UV lamp in order to minimise the effects of overlapping exposures to multiple UV lamps. Tension, compression and DMA samples printed lengthwise along the X-, Y- and Z-directions will be referred to as X-, Y-, and Z- respectively from hereon (Figure 1). All samples were printed with the matte finish option as the glossy finish could potentially lead to tougher samples due to over-curing [43]. This meant that each part was coated with support material regardless of overhang criteria and orientation. The support material used was SUP706, a soluble acrylic wax, which was later removed with a water jet. A cleaning tank with a sodium hydroxide solution was not used as it was found to warp thin walls and delicate edges. Layer thickness was confirmed to be 16 microns through scanning electron microscopy measurements of specimen cross sections (Appendix A).

Tension and compression tests were carried out on the elastomers to determine their quasi-static response for hyperelastic modelling and to assess their strain rate sensitivity. Stress relaxation tests and DMA were conducted to assist in understanding and modelling of the time- and temperature-dependent mechanical behaviour of the elastomers.

Tension

Tension samples were dumb-bell pieces (Figure 1) with a narrow section (33 mm length; 6.2 mm width; 2 mm thickness) as per BS ISO 37:2017 Type 1 [50]. At least three specimens were tested for each orthogonal print direction and respective strain rate to ensure results showed good repeatability. Sample gauge sections were then marked for strain measurements for the assistance of image tracking.

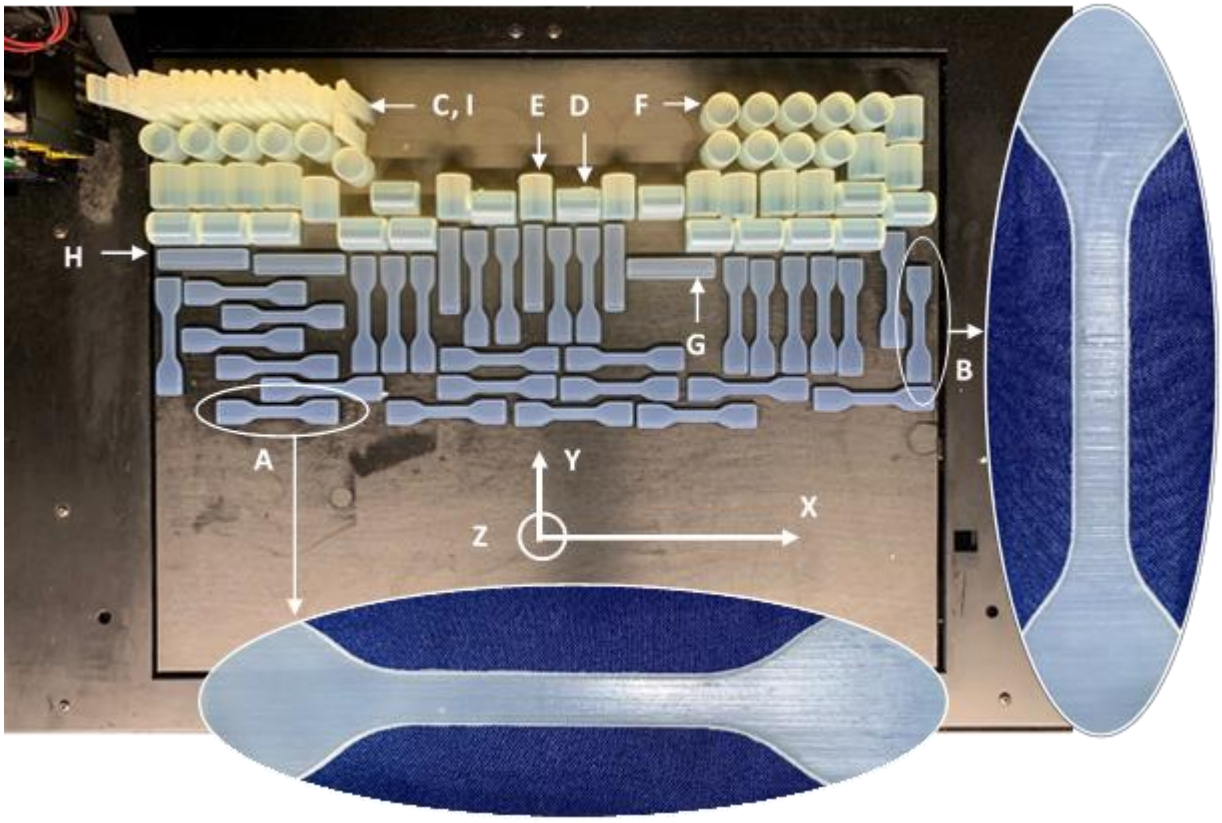


Figure 1 - Stratasys Connex3 Objet500 printer bed with printed X- Y- and Z- tension (A, B and C respectively), compression (D, E and F) and DMA (G, H and I) samples. Streaks left by the PolyJet printing process can be seen lengthwise along the X- tensile sample (A) and along the width of the Y- sample (B).

An electromechanical Instron Universal Testing System (Instron 5543, Instron) with a 1kN load cell was used for uniaxial tension and compression tests on pristine samples. Pneumatic side-action grips were used for the tension tests to allow for a consistent pressure distribution on the ends of the specimen during testing preventing specimen slippage. This is particularly important for elastomers with a large failure strain as thinning at the ends of the specimen can lead to loss of grip and eventual slipping. All samples were tested within 1 day of printing.

Five discrete strain rates spanning two orders of magnitude were achieved for both tension and compression tests. In tension, strain rates of 0.003, 0.015, 0.30, 0.15 and 0.3 /s were achieved. This provided the three-dimensional material response of stress vs. strain vs. strain rate for each of the orthogonal print directions.

Compression

Compression samples were cylindrical specimens (17.8 mm diameter; 25 mm height) as per BS ISO 7743:2017 Type B [51]. Nut-locking compression platens were used for unconfined compression tests to ensure platen translation or rotation did not occur during tests. Platen surfaces were lubricated with oil to ensure homogenous compression and minimise specimen barrelling effects. Crosshead speeds were set to achieve engineering strain rates of 0.005, 0.025, 0.05, 0.25 and 0.5 /s.

Cyclic Loading

Cyclic loading tests on pristine samples with the same dimensions were carried out to assess recoverability of the elastomers and hence whether a visco-hyperelastic material model would be more suitable than a visco-plastic model at this range of strain rates. The samples were compressed to an engineering strain of 0.6, then immediately unloaded to zero extension. Reloading was then either immediately initiated or initiated after 20 seconds of idle time.

Stress Relaxation

The stress relaxation tests were initiated by a constant compression rate to 0.05, 0.1 and 0.2 engineering strains, with a ramp time of 1.5 seconds, followed by a 100 second hold period. The relaxation results were later used to calibrate a Prony series used in the material model.

Dynamic Mechanical Analysis

DMA samples were bar shaped (10 mm width; 2.5 mm thick; 35 mm effective gauge length; 55 mm total length) for dual-cantilever clamps on a TA Q800 DMA tester (Figure 2) as per the guidelines of TA Instruments [52]. The DMA tester was used in dual-cantilever mode for the storage modulus (E'), loss modulus (E'') and loss tangent ($\tan(\delta)$) measurements of the elastomers related by:

$$\tan(\delta) = \frac{E''}{E'} \tag{1}$$

Where δ is the phase lag between the applied strain wave ($\varepsilon(t)$) and measured stress wave ($\sigma(t)$). When the phase lag increases from an elastic state, where both waves are perfectly in phase ($\delta = 0°$), to a viscous fluid state, when both waves are perfectly out of phase ($\delta = 90°$), the loss modulus increases and storage modulus decreases [53]. Hence:

$$E' = \frac{\sigma_{peak}}{\varepsilon_{peak}}\cos(\delta) \; and \; E'' = \frac{\sigma_{peak}}{\varepsilon_{peak}}\sin(\delta) \tag{2}$$

The $\tan(\delta)$ peak determined from DMA results, which occurs when the ratio between the loss modulus and the storage modulus is highest, gave indications of the glass transition temperature (T_g) of the elastomers [53].

The first stage of DMA testing was initiated at 80°C wherein each sample was loaded with an oscillatory load frequency of 1Hz in the position shown in Figure 2. During this testing stage, each sample was cooled down to -80°C at a rate of -2°C, thus showing how the moduli E' and E'' changed with temperature. The second stage of DMA testing involved a frequency sweep (from 1Hz - 100Hz) at discrete temperature steps 5°C apart starting at 5°C to 20°C. The Williams-Landel-Ferry shift function was used to obtain the time-temperature superposition (TTS) master curves (Eq. (3)).

$$\log(\alpha_T) = -\frac{C_1(T - T_r)}{C_2 + (T - T_r)} \tag{3}$$

The shift factor (α_T) is a temperature-dependent multiplier of the oscillatory test frequency at the temperature T that corresponds to a 'new' equivalent frequency at the reference temperature ($T_r = 20°C$) [54]. C_1 and C_2 are material-dependent constants which we determined through a curve-fitting routine [54,55] and reported in the Results section.

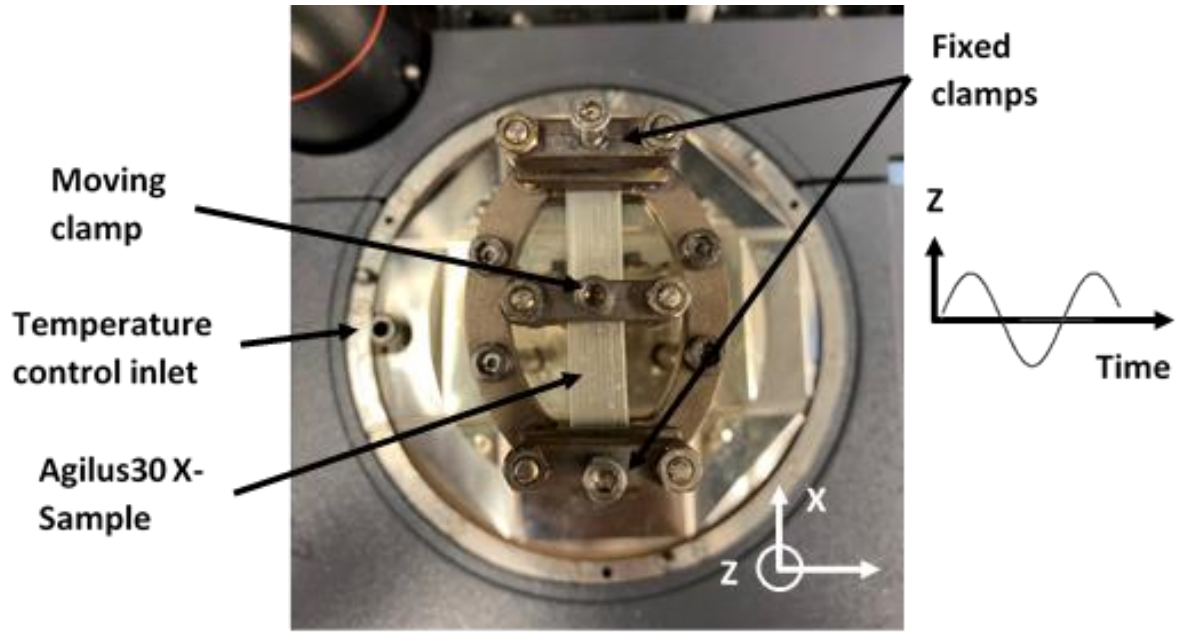


Figure 2 - TA Q800 DMA tester setup with x-direction A30 specimen on the dual-cantilever clamp.

Numerical Methods

Hyperelasticity

To numerically model the observed visco-hyperelastic material behaviour, isotropy was assumed to allow for characterisation using a well-established strain energy function proposed by Ogden et al. [56] (Eq. (4)). This also allows for relatively easy implementation into FE codes [57,58]. The Ogden strain energy function is given by:

$$W = \sum_{i=1}^{N} \frac{\mu_i}{\alpha_i}\left(\lambda_1^{\alpha_i} + \lambda_2^{\alpha_i} + \lambda_3^{\alpha_i} - 3\right) + \frac{K}{2}(J - 1), \tag{4}$$

where λ_1, λ_2, λ_3 are the deviatoric (volume-preserving) principal stretches, μ_i are moduli and α_i are non-dimensional material constants. K and J are the material bulk modulus and the elastic volume ratio respectively. Elastomers are often assumed incompressible ($J \cong 1$) and therefore the second term is disregarded [27,53,59–61]. This leads to the engineering (nominal) stress expression for uniaxial deformation (σ_{11}) where $\lambda_2 = \lambda_3 = \lambda_1^{(-1/2)}$:

$$\sigma_{11}^H = \frac{\partial \overline{W}}{\partial \lambda_1} = \sum_{i=1}^{N} \mu_i \left({\lambda_1}^{\alpha_i - 1} + 2{\lambda_1}^{\frac{-\alpha_i}{2} - 1} \right) \tag{5}$$

The trust-region-reflective algorithm in MATLAB was used to determine the constants μ_i and α_i by calibrating the quasi-static material model in Eq. (5) to the experimental tension-compression stress-strain response at the lowest strain rate. The X- sample mechanical responses were chosen for this characterisation. Errors arising from this choice depend on the print direction and predominant mode and rate of loading of the printed part as explored later in this paper.

Visco-hyperelasticity

A convolution integral was used to model the time-dependent behaviour of the PolyJet elastomers, which is commonly employed to describe the linear viscoelastic stress response of elastomers and biological tissue [53]:

$$\sigma^{VH}(t) = \int_0^t g(t-s) \frac{\partial \sigma_0^H}{\partial s} \partial s. \tag{6}$$

Where σ_0 is the instantaneous hyperelastic stress which fades into the quasi-static stress (σ_∞) exponentially with time (t) as time tends to infinity i.e. $t \to \infty, \sigma(t) \to \sigma_\infty$. Hence, $g(t-s)$ is a normalised relaxation function ($0 < g(t-s) < 1$) that is modelled here as a generalised Maxwell element expressed in terms of a Prony series of exponentials [57,62,63]:

$$\sigma^{VH} = \int_0^t \left(g_\infty + \sum_{i=1}^{n} g_i e^{-\frac{t-s}{\tau_i}} \right) \frac{\partial \sigma_0^H}{\partial s} \partial s = \underbrace{g_\infty \sigma_0}_{\sigma_\infty^H} + \int_0^t \left(\sum_{i=1}^{n} g_i e^{-\frac{t-s}{\tau_i}} \right) \frac{\partial \sigma_0^H}{\partial s} \partial s \tag{7}$$

τ_i is the characteristic relaxation time pairing with g_i, where g_i is the normalised ith elastic moduli (E_i).:

$$g_i = \frac{E_i}{E_0} = E_i / (E_\infty + \sum_{i=1}^{n} E_i) \tag{8}$$

Where E_0 and E_∞ are the instantaneous and quasi-static elastic moduli respectively.

Three Prony pairs (g_i,τ_i) were approximated from the stress relaxation tests using a nonlinear least-squares fit where $1 \leq \tau_i \leq 100$ s. For smaller timescales ($\tau \leq 0.1$ s), the stress relaxation tests become less appropriate to approximate relaxation parameters due to the dynamic effects resulting from crosshead acceleration that confound the results. Therefore, Prony pairs for $\tau \leq 0.1$ s were evaluated from DMA time-temperature superposition master curves using a MATLAB code employing the Levenberg-Marquardt method described in more detail in Appendix E [64].

Numerical Time-stepping Scheme

A closed-form for the convolution integral solution in Eq. (7) is often difficult to obtain, particularly when advanced strain energy functions with various strain histories are applied. Therefore, a method using finite time increments proposed by Taylor et al. [65] was implemented to solve the integral.

$$\sigma^{VH}(t_{n+1}) = \underbrace{\sigma_{\infty}^{H}(t_{n+1})}_{elastic\ comp.} + \underbrace{\sum_{i=1}^{n}\left(\exp\left(-\frac{\Delta t}{\tau_i}\right) h_i(t_n) + \frac{g_i \dfrac{1-\exp\left(-\frac{\Delta t}{\tau_i}\right)}{\frac{\Delta t}{\tau_i}} [\sigma_{\infty}^{H}(t_{n+1}) - \sigma_{\infty}^{H}(t_n)]}{g_{\infty}} \right)}_{viscoelastic\ component}$$

$$\therefore \sigma^{VH}(t_{n+1}) = \sigma_{\infty}^{H}(t_{n+1}) + \sum_{i=1}^{n} h_i(t_{n+1}) \quad (9)$$

The first term relates to the hyperelastic (time-independent) stress (σ_{∞}^{H}) obtained from the 3-term Ogden model parameters fit to the quasi-static tests (Eq. (5)). The second term describes the summation of the viscoelastic (time-dependent) stress contribution ($\sum_{i=1}^{n} h_i$). A detailed derivation can be found in [63,66]. Using this time-stepping scheme, we evaluated the stress at each interval of time at discrete strain rates and compared to the monotonic tension and compression test data to determine the accuracy of the material model predictions across a range of strain rates.

Results

Experimental Results

We found highly repeatable results across all tests, with small standard deviations (see Appendix B for tension and Appendix D for relaxation and DMA repeat results). Standard deviation (SD) values are reported in tables rather than on the graphical results as SD bars were too small to visualise.

Tension

The tensile response followed a general S curve with an initial stiff region up to a strain of 20%, followed by a softer response (Figure 3). This behaviour was more pronounced at higher strain rates (0.3 /s), where the response became increasingly nonlinear. A rise in the stress response prior to failure was observed at higher strain rates due to chain limiting extensibility as failure strain increases.

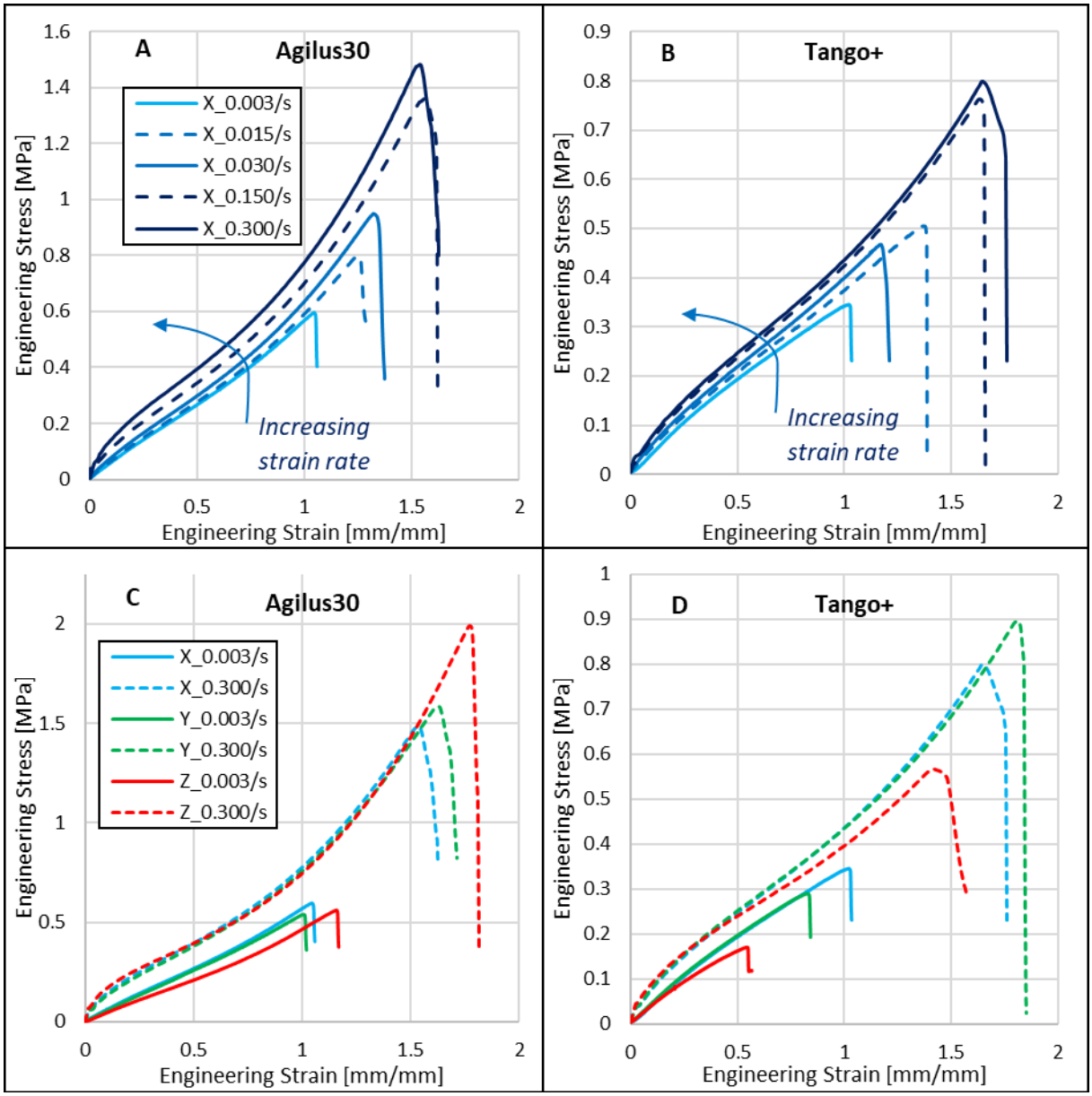


Figure 3 - Tensile stress-strain results showing the effects of strain rate on A30 (A) and T+ (B) and the effects of build orientation on A30 (C) and T+ (D)

Z- samples in both materials were softer across all strain rates below 0.3 /s, particularly at strains larger than 50% (Figure 3C,D and Table 1). For A30, Z-sample stress values at 50% strain during the 0.03 /s tests were significantly lower than X- ($t(3)=8.63$, $p<0.001$), whereas Y- samples were not ($t(3)=1.24$, $p=0.28$). A similar observation was made for T+ ($p<0.005$ and $p=0.12$ for Z- and Y-samples respectively).

Interestingly, the offset between Z- stress responses and the other two orthogonal print directions decreases with increasing strain rate, particularly for A30. This trend was observed in both materials. In fact, the response at 20% strain was marginally stiffer in Z- than X- and Y-samples at the highest strain rate (Figure 3C,D).

To better quantify the effects of print direction on stress responses, we determined the stress at 50% strain across all strain rates for both materials and compared them (Table 1). For A30, increasing the strain rate from 0.003 to 0.3 /s increased the tensile stress at 50% strain by 67% for X and Y-samples. This increase was almost twice as large for Z-samples, primarily due to their softer response at lower strain rates. In comparison to A30, T+ had lower strain-rate sensitivity across all loading directions.

Table 1 - Nominal stress values at 50% tensile strain of A30 and T+ at various strain rates

Stress [MPa] v. Strain rate [/s]	**0.003 /s**	**0.015 /s**	**0.03 /s**	**0.15 /s**	**0.3 /s**	**% increase. 0.003 - 0.3 /s**
			A30			
50% strain: X	0.174	0.182	0.202	0.245	0.291	**67%**
(±SD)	0.004	0.005	0.006	0.001	0.004	
Y	0.163	0.193	0.187	0.242	0.273	**67%**
(±SD)	0.011	0.003	0.016	0.006	0.002	
Z	0.135	0.149	0.158	0.226	0.306	**127%**
(±SD)	0.003	0.001	0.004	0.026	0.027	
			T+			
50% strain: X	0.194	0.208	0.220	0.241	0.248	**28%**
(±SD)	0.004	0.002	0.001	0.002	0.003	
Y	0.197	0.207	0.222	0.238	0.259	**31%**
(±SD)	0.003	0.002	0.001	0.006	0.005	
Z	0.164	0.180	0.192	0.220	0.241	**47%**
(±SD)	0.004	0.005	0.006	0.002	0.013	

In order to better show the effects of strain rate and build orientation on ultimate tensile stress and strain, we plotted them against each other for both A30 and T+ (Figure 4). We found that ultimate tensile stress and strain of both materials increased with strain rate. All samples were re-measured 20 minutes after testing to failure, and no residual strain was observed, indicating the material was fully elastic up to failure (Appendix A).

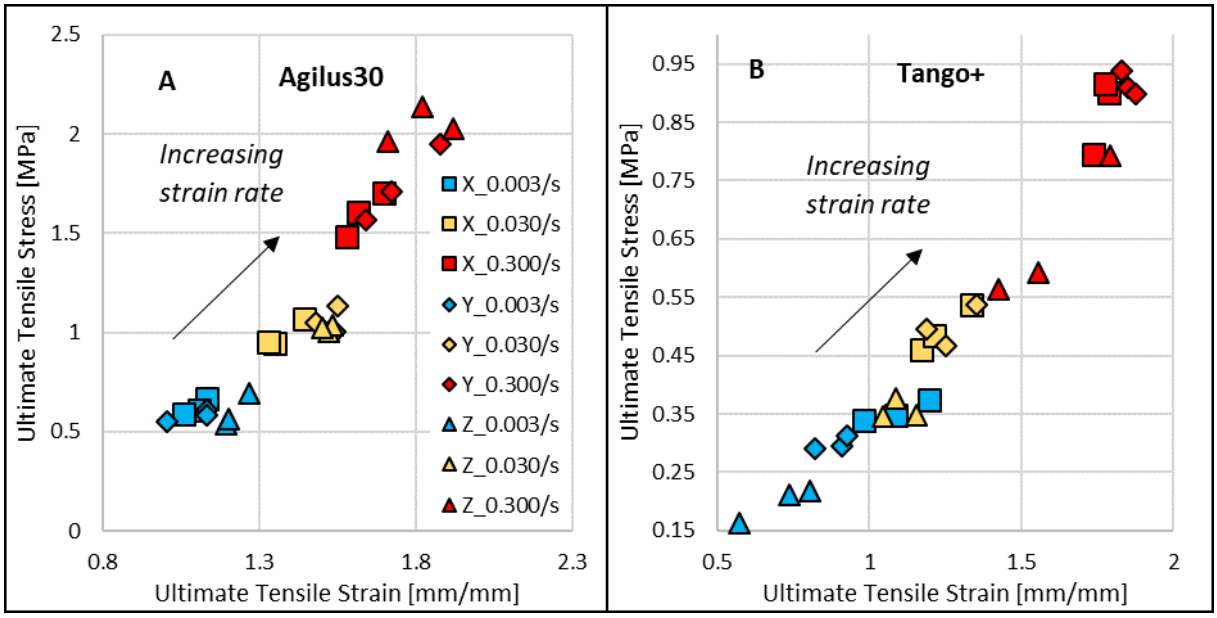


Figure 4 – Ultimate tensile stress and strain of A30 (left) and Tango+ (right) at various strain rates

Compression

Compressive loading and unloading stress-strain paths were influenced by strain-rate in both materials (Figure 5). An initial stiffness was followed by a yield-like stress-rollover at strains of ~0.05, which was more pronounced at higher strain rates, however less so with T+ than A30 (Figure 5). The dissipated work density (DWD), defined as the area under the stress-strain curve, was larger for A30 than T+, and more influenced by strain rate in A30. We evaluated the DWD as [67,68]:

$$DWD = \int_0^{\varepsilon_{max}} \sigma_{load}\, d\varepsilon - \int_{\varepsilon_{max}}^{\varepsilon_{(0)}} \sigma_{unload}\, d\varepsilon \qquad (10)$$

Our results show that the dissipated work density with T+ increases by almost 10 folds, and nearly 17 folds for A30, when the strain rate is increased by two orders of magnitude (Table 2).

Table 2 - Dissipated work density (DWD) of A30 and T+ in compression at various strain rates.

Dissipated work density [MPa] vs. Strain rate	**0.005 /s**	**0.025 /s**	**0.05 /s**	**0.25 /s**	**0.5 /s**	**% increase. 0.005 - 0.5 /s**
A30						
X	0.065	0.133	0.185	0.375	0.610	**838%**
(±SD)	0.001	0.005	0.001	0.002	0.003	
Y	0.054	0.114	0.161	0.359	0.583	**979%**
(±SD)	0.002	0.002	0.004	0.001	0.002	
Z	0.056	0.110	0.174	0.374	0.594	**960%**
(±SD)	0.003	0.001	0.002	0.002	0.004	
T+						
X	0.019	0.061	0.087	0.206	0.288	**1416%**
(±SD)	0.001	0.004	0.001	0.003	0.006	
Y	0.015	0.051	0.085	0.180	0.261	**1640%**
(±SD)	0.005	0.002	0.001	0.003	0.002	
Z	0.016	0.056	0.079	0.205	0.272	**1700%**
(±SD)	0.001	0.004	0.002	0.002	0.002	

Print direction also had a significant influence on the stiffness in compression. A30 Z- samples were significantly softer than X- at 50% strain during the 0.005 /s tests ($t(3)=4.72$, $p=0.01$), whereas the difference between X- and Y- samples was less significant ($t(3)=2.57$, $p=0.06$). This difference is more pronounced at lower than at higher strain rates, particularly in A30 (Figure 5C,D). A similar observation was made in tension (Figure 3C,D) regarding the difference between Z- samples and other build orientations across strain rates.

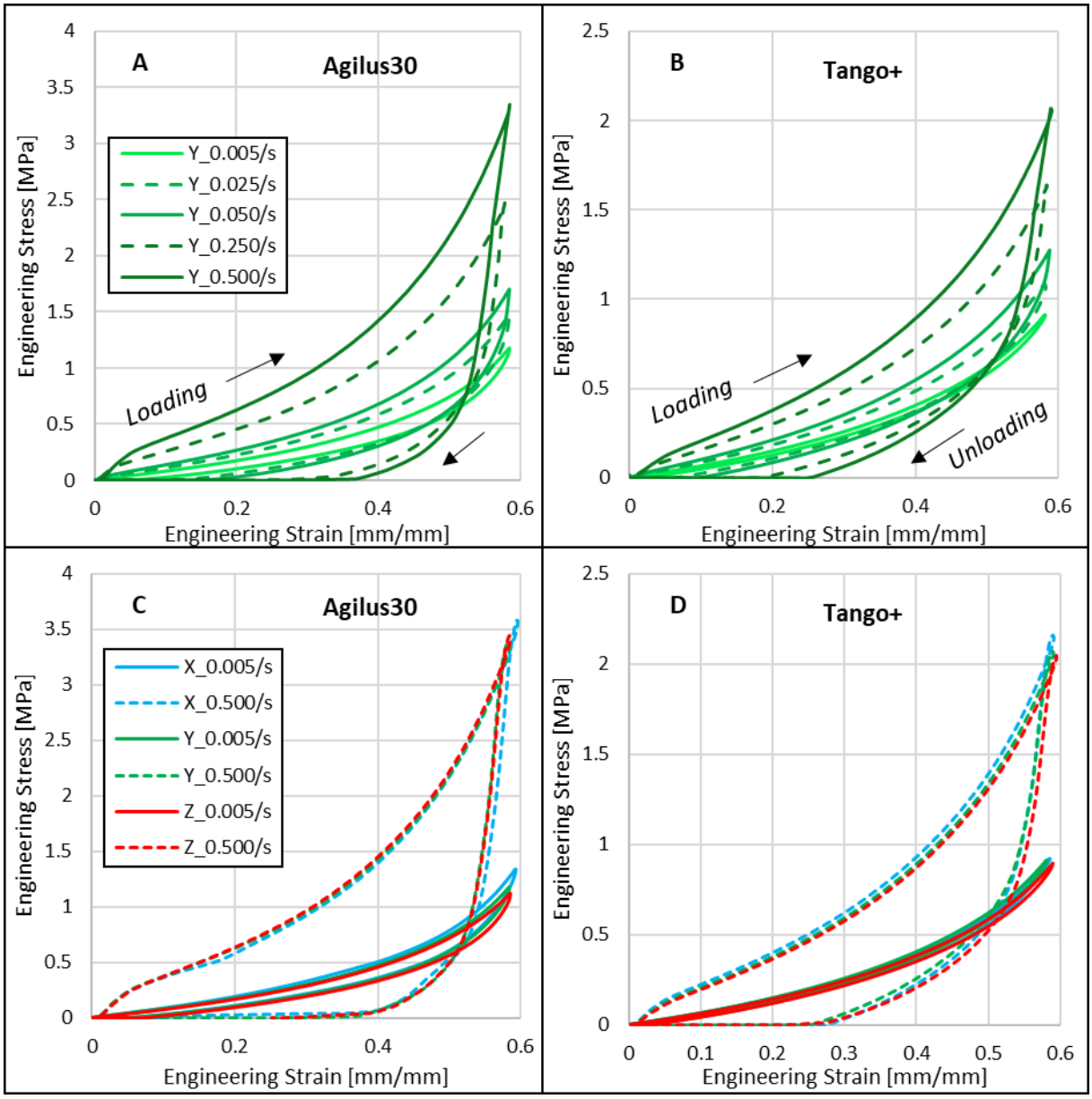


Figure 5 - Compressive loading and unloading stress-strain results for A30 (A) and Tango+ (B) Y- samples at varying strain rates. Comparison between compressive stress-strain responses of A30 (C) and Tango+ (D) X-, Y- and Z- samples at the lowest and highest strain rates.

Cyclic Loading

Cyclic test results did not show any permanent plastic deformation, which indicates visco-hyperelastic behaviour rather than visco-plastic (Figure 6). With immediate reloading (blue), A30 had a residual strain of 0.16 in the first cycle and 0.18 in the second cycle. In contrast, T+ samples had a residual strain of 0.09 after the first cycle and 0.1 after the second. When a 20 second idle time lapsed before reloading, both materials fully recovered to their original height, diminishing the residual strain.

Cyclic softening was observed with every subsequent loading cycle with A30, but the softening was less pronounced at lower strain rates (Appendix C). Notably, the unloading path of both materials was less affected by the cyclic loading and idling conditions in contrast to the loading path.

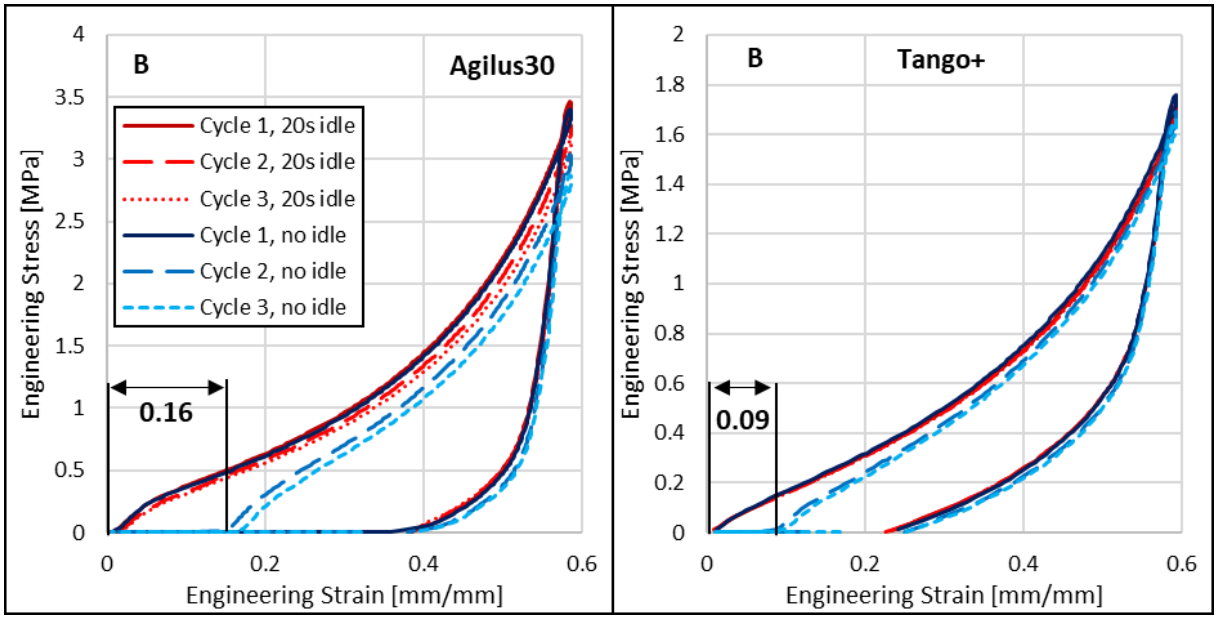


Figure 6 - Cyclic loading of A30 and Tango+ X- samples at strain rates 0.05 /s (blue) and 0.5 /s (red).

Stress Relaxation

Stress relaxation profiles at 5% - 20% strain normalised by peak stress showed a remarkable overlap for both materials (Figure 7A). Overlapping the normalised profiles of both materials highlights the difference between their characteristic relaxation times. A30 relaxes to more than 50% of the peak stress 20 seconds after the ramp load, whereas T+ relaxes to 70% (Figure 7A). As highlighted by the exemplar results of A30, the relaxation behaviour of both materials showed no significant relationship with build orientation (Figure 7B).

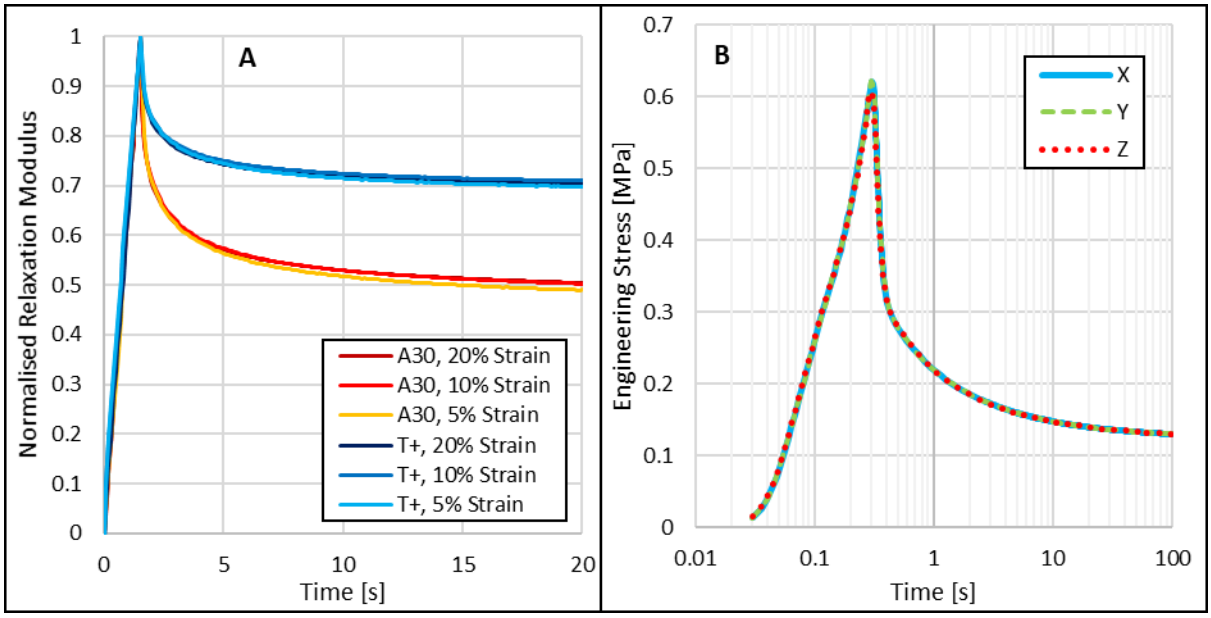


Figure 7 – Normalised relaxation profiles for A30 and T+ samples at different strain levels (A). Stress relaxation results for X- , Y- and Z- A30 samples at 20% strain with a 0.3 s ramp time (B).

Dynamic Mechanical Analysis (DMA)

DMA temperature sweep and time-temperature superposition results of both materials showed similar trends in storage modulus and loss tangent (Figure 8), with a continuous decay in storage modulus and one peak in loss tangent near $\sim 0°C$. The peak in loss tangent indicates the glass transition temperature (T_g).

Z- samples for both materials had a left-shifted average $\tan(\delta)$ and E' curves and lower $\tan(\delta)$ average peak values. Although these findings reinforce the discrepancies found in Z- samples reported for other tests, the differences in Z- T_g in comparison to X- were not significant (t(3)=1.55, p=0.19 for A30, t(3)=1.5, p=0.20 for T+). Similarly, the difference in T_g of Y- and X- samples were not significant (t(3)=-0.31, p=0.77 for A30, t(3)=-0.5, p=0.64 for T+).

Williams-Landel-Ferry shift constants $C_1 = 10.5, C_2 = 100$ (Eq. (3)) were found to provide a remarkably good fit for E', E'' and $\tan(\delta)$ master curves (Figure 9). E' and E'' master curves were later used to calibrate the Prony series parameters of the numerical model for time-scales below $\tau \leq 0.1$s (Appendix E).

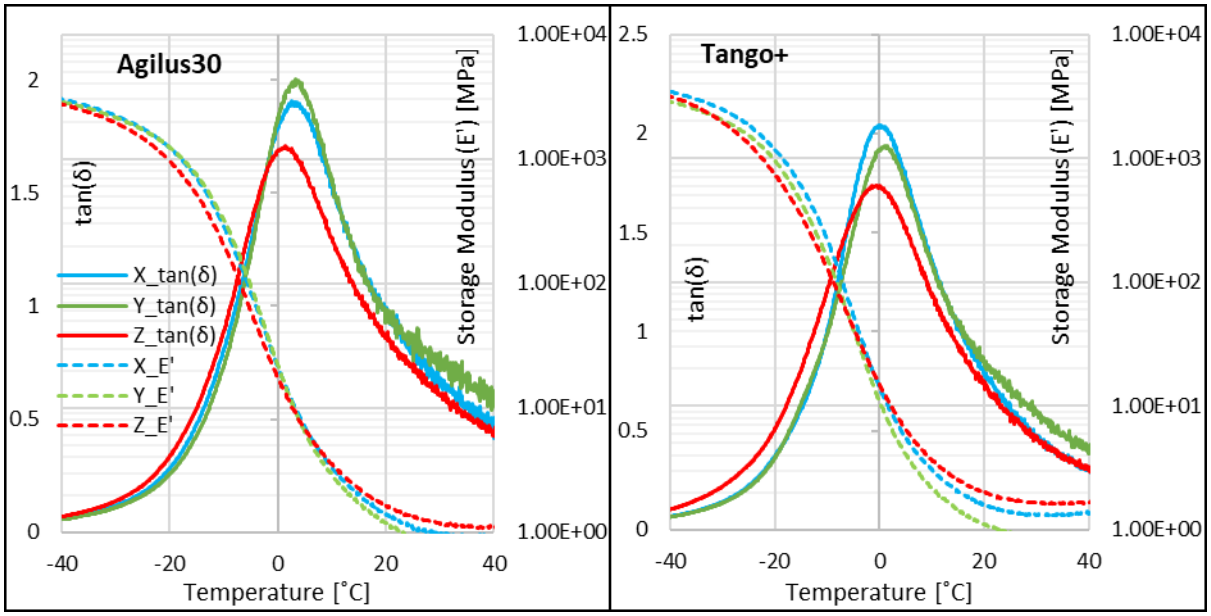


Figure 8 - DMA loss tangent and storage modulus (E') results temperatures relevant to glass transition of A30 (left) and Tango+ (right) samples printed in different orientations.

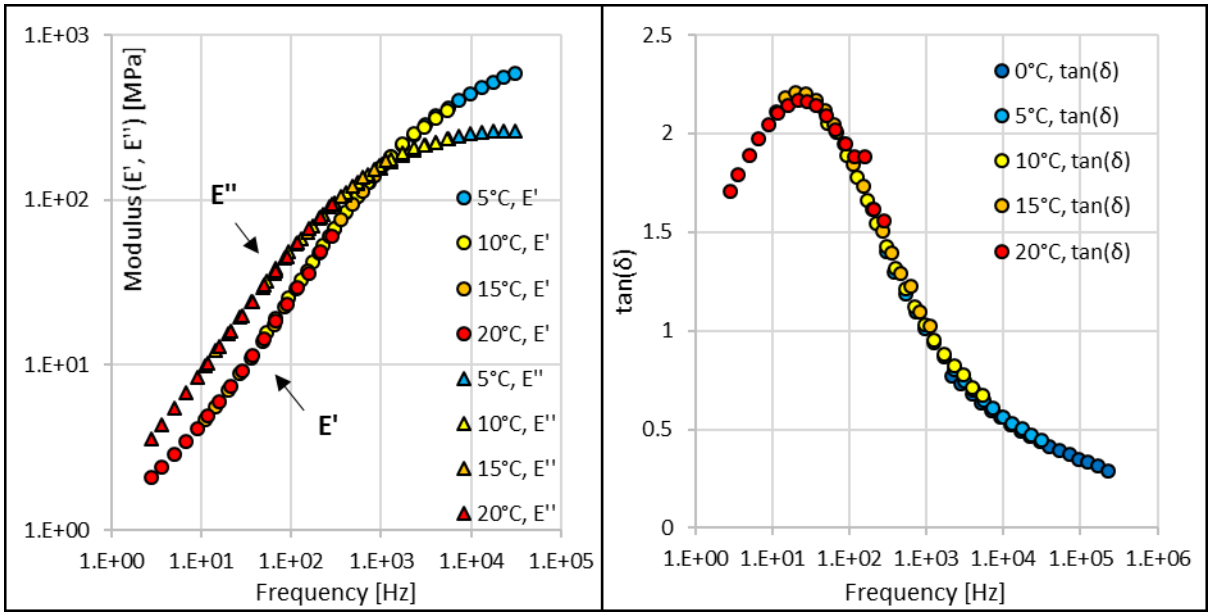


Figure 9 - DMA TTS frequency-domain storage (E') and loss (E'') moduli (left) and loss tangent (right) master curves for A30 shifted using Williams-Landel-Ferry shift constants C_1=10.5, C_2=100.

Model predictions of stress relaxation responses

The Prony series coefficients determined from the stress relaxation tests allowed us to model the relaxation response with remarkable accuracy (Figure 10). The determined Prony series coefficients for A30 and T+ are reported in Table 4. To quantify the accuracy of the numerical model, the root mean squared percentage error (RMSPE) was calculated as:

$$RMSPE = \frac{100}{n}\sum_{i=1}^{n}\sqrt{\frac{\left(y_{i(ref)} - y_{i(pred)}\right)^2}{y_{i(ref)}}} \quad (11)$$

$y_{i(ref)}$ and $y_{i(pred)}$ are the experimental and numerically predicted result points. The RMSPE for 100s stress relaxation tests was 0.5% and 3.5% for A30 and T+ respectively (Table 5).

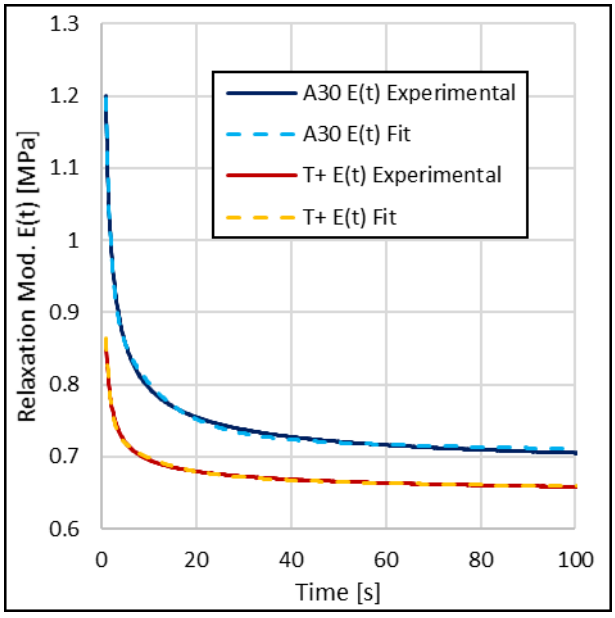


Figure 10 – Relaxation modulus of our Prony series prediction overlaid on the experimental results of A30 and T+ from a 100s relaxation test.

Model predictions of tension and compression responses at different strain rates

The Ogden and Prony series parameters of the visco-hyperelastic model for both materials, which were determined using the quasi-static tension-compression and DMA test results, are reported in Table 3 and Table 4 respectively. These parameters were used to predict the stress-strain response of the material in tension and compression at different strain rates. The model generally predicts the response of both elastomers well across 0.003 to 0.5 /s strain rates (Figure 11).

To assess the performance of the model against other build directions, we calculated the RMSPE of the model in comparison to Y- and Z- samples at each compressive and tensile strain rate for both materials (Table 5). The error was largest in compressive loading at the highest strain rate. Our results show that RMSPE varied between 1.3% and 13% for tension and 7.8% and 16.1% for compression of X- samples across both materials (Table 5). The RMSPE is largest with Z- samples at 0.003 /s strain rate (RMSPE=29.9%) as Z- samples were significantly softer than X- and Y- samples at lower strain rates.

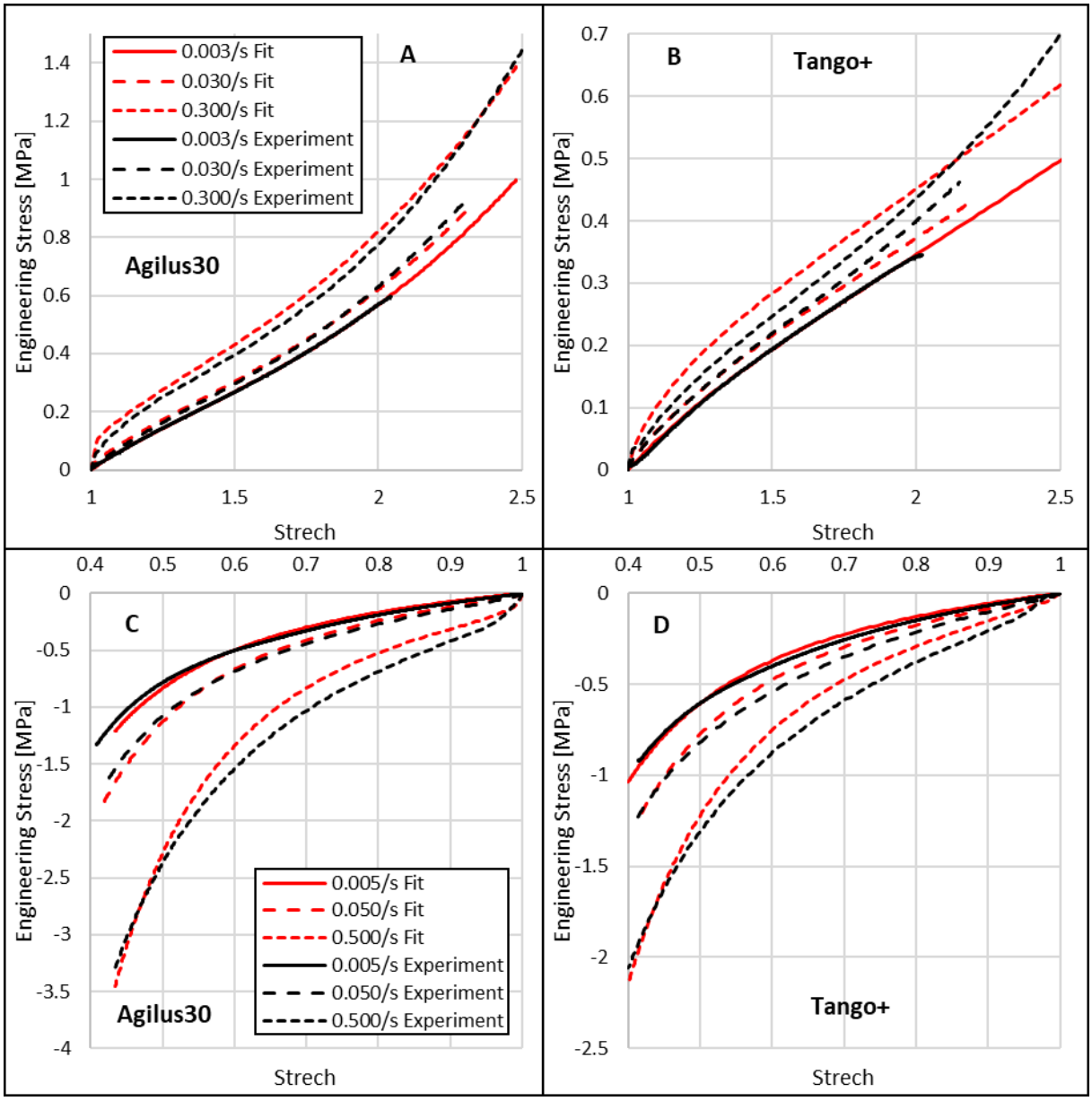


Figure 11 - The visco-hyperelastic material model prediction vs. experiment for A30 and T+ tensile (A,B) and compressive (C,D) responses at various strain rates.

Table 3 - Ogden quasi-static hyperelastic material parameters for A30 and T+.

	$\mu_1(\infty)$ [MPa]	α_1	$\mu_2(\infty)$ [MPa]	α_2	$\mu_3(\infty)$ [MPa]	α_3
A30	0.2127	1.3212	0.0375	4.318	-0.001	-1.0248
T+	0.1211	2.4061	0.0209	2.408	-0.001	-1.0011

Table 4 - Prony parameters for visco-hyperelastic material model for A30 and T+.

A30	g_i	8.38E-01	1.26E-01	1.03E-02	3.00E-03	4.39E-04
	τ_i [s]	5.08E-03	4.97E-02	1.00E+00	1.00E+01	1.00E+02
T+	g_i	7.37E-01	1.05E-01	4.67E-02	1.07E-02	3.59E-03
	τ_i [s]	9.24E-03	1.73E-01	1.00E+00	1.00E+01	1.00E+02

Table 5 - Root Mean Square Percentage Error (RMSPE) of the visco-hyperelastic model prediction for all tests on A30 and T+.

	A30			T+		
Tension	**0.003 /s**	**0.03 /s**	**0.3 /s**	**0.003 /s**	**0.03 /s**	**0.3 /s**
X RMSPE [%]	1.3	10.5	7.5	3.1	4.4	13.0
Y RMSPE [%]	6.1	5.6	13.9	2.7	4.2	10.3
Z RMSPE [%]	29.9	26.7	12.8	15.2	18.9	12.02
Compression	**0.005 /s**	**0.05 /s**	**0.5 /s**	**0.005 /s**	**0.05 /s**	**0.5 /s**
X RMSPE [%]	11.3	7.8	16.8	11.6	10.8	16.1
Y RMSPE [%]	9.3	7.4	13.7	12.6	12.7	15.9
Z RMSPE [%]	7.8	6.3	13.0	9.2	4.3	16.1

Discussion

We determined the mechanical response of two newly developed Polyjet elastomers, A30 and T+, across a wide range of strain and strain rates and along different build orientations. We conducted a comprehensive set of tests including uniaxial tension-compression at discrete strain rates, stress relaxation tests, DMA and cyclic loading, which allowed us to explore the mechanical responses of these digital elastomers. For the first time, we employed a visco-hyperelastic material model to accurately predict the stress-strain response of the elastomers at a range of tensile and compressive strain rates. Our comprehensive experimental data allowed us to determine the constants of this material model. The model utilises a widely used 3-term Ogden hyperelastic strain energy function alongside a 5-term Prony series to model viscoelastic effects in a manner readily compatible with major FEA codes, such as Abaqus and LS-Dyna, allowing for ease of implementation.

We found that the ultimate tensile strength of the elastomers increased with increasing strain rate. This is in agreement with previous studies which reported increased strain at failure and fracture energy at higher strain rates for older PolyJet elastomers; Tango [27,49]. This dependency may be due to entangled dynamics of polymer chains at higher strain rates, which lead to a delayed onset of failure. We noted that many of the tensile failures were near the corners of the gauge section as noted in [36], and thus ultimate tensile strength varied between repeat tests leading to SDs as high as 19.3% (T+ Z- samples, 0.3 /s). This observation is most likely due to the stress concentrations near the region arising from the pixelated approximation of curves in the printing process. Hence, ISO/ASTM sample shapes for determining tensile properties of moulded or cast rubbers may not be appropriate for testing AM rubbers, and development of new tensile sample shapes or testing methods that address the stress concentrations near pixelated edges of PolyJet elastomers may be necessary.

We determined the loss and storage moduli across a wide range of frequencies using DMA, allowing us to characterise the relaxation modulus for a wide time span (10 µs - 100 s). Our results are in good agreement with previous work that has reported loss and capture modulus for A30 at a limited frequency range [14]. For the first time we broadened the DMA with the time-temperature superpositioning and determined Williams-Landel-Ferry shift function constants (C_1, C_2) for A30 and T+. These constants characterise the unique time-temperature dependency of the elastomers, and therefore can easily be extended to other methods such as creep tests [53,59], analogous to relaxation tests reported here.

The reported DMA results show a high glass transition temperature (T_g) for both materials (nearly $0°C$). The high T_g may limit the suitability of these elastomers in applications where material properties are expected to remain constant with temperature change, a role currently fulfilled by commercial elastomers such as thermoplastic polyurea and polyurethane (TPU) [61,67,69–71]. Nonetheless, PolyJet elastomers have been granted attention in the domain of energy absorption, such as bio-inspired composite armour [29], due to their readiness for multi-material 3D printing. Moreover, the high T_g is also why PolyJet elastomers have dominated applications in 4D printing and active composites utilising thermomechanical programming processes [14,19,23].

The mechanical responses of both A30 and T+ were highly nonlinear and time-dependent across the range of strain rates. The nonlinear and rate dependent behaviour observed in both materials is common of amorphous polymers and may be attributed to molecular chain dynamics [59,72]. Conventional co-polymers such as TPU also show similar trends in stress-strain profiles with increasing strain rate. In addition, we observed an initial high stiffness at higher strain rates, followed by a pronounced yield-like stress-rollover at small strains (~0.05). Similar observations about TPU have been reported previously, which have been attributed to the interplay between 'hard' and 'soft' molecular domains within the polymer network [67,72].

Our relaxation tests assisted in determining the Prony series coefficients, and hence our visco-hyperelastic material model can predict the time-dependent behaviour of both materials with reasonably good fidelity. Previous methods used the stress-strain responses of uniaxial tensile tests at discrete strain rates to calibrate the Prony series coefficients instead of directly calibrating to relaxation tests [27,73]. However, such methods do not guarantee an accurate prediction of the relaxation profiles of the materials as illustrated in Figure 12, regardless of the capability of a model to predict the uniaxial response at discrete strain rates. Hence, we accompany the discrete strain rate tests with stress relaxation tests to determine the material model coefficients, which in turn provides a realistic representation of both uniaxial and relaxation test responses.

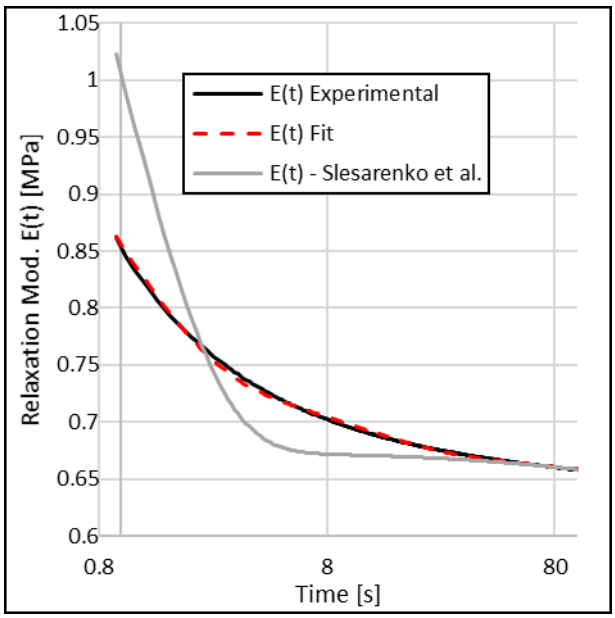


Figure 12 – Comparison between the relaxation test results and our Prony series prediction and that reported in [27].

The basis of the convolution integral that we used for numerical modelling is the assumption of separable time- and strain-dependent material behaviour. This assumption is widely accepted for

many viscoelastic materials including cheese and bread dough [63,74]. We accepted this assumption based on the remarkable overlap of the stress relaxation profiles at varying strain levels (Figure 7). This observation shows that the relaxation response of the PolyJet materials is independent of the applied strain, and hence the assumption of separable time- and strain-dependent behaviour is plausible.

The Ogden hyperelastic model was chosen to characterise the quasi-static response of A30 and T+. This model is well established and utilises a few parameters, and it accurately predicted the hyperelasticity of both elastomers. However, the Ogden hyperelastic function is isotropic. Hence, isotropy was assumed for numerical modelling and therefore was fit to X- sample data as incorporating an anisotropic visco-hyperelastic model would significantly complicate the model and lead to difficulty in application. Nonetheless, the model was still able to predict the response of both materials in Y- and Z- build direction with good accuracy apart from Z- samples at 0.003 /s strain rate where Z- samples were significantly softer. This observation was expected as we previously noted that Z- were significantly softer than X- samples which were used for numerical modelling. Interestingly, the RMSPE of Y- and Z- samples is even lower than X- in compressive loading at 0.3 /s strain rates as anisotropy diminished at higher strain rates. As mentioned, the importance of anisotropy is application specific as it depends on the strain, strain rate and loading mode. Slender load bearing members are typically not recommended to have their primary loading directions along the Z- print axis as printing strength diminishes and build time significantly increases with Z- height and in most AM methods. Nonetheless, the prediction errors were reasonable, indicating that this model will perform reliably when employed e.g. in FEA simulations of large strain problems within the range of strain rates explored here.

Our experimental results on the effect of build orientation on anisotropy of T+ and A30 PolyJet elastomers at large strains with varying strain rates adds to the existing knowledge on anisotropy of PolyJet parts. As anisotropy is often regarded as a limiting factor for the performance and reliability of AM materials and methods, it has attracted much research, however less so for the PolyJet elastomers explored here, in contrast to plastics. Our findings on anisotropy are in line with previous reports on PolyJet plastics suggesting that Z- specimens had the poorest mechanical properties [40,42–44]. However, we conclude that anisotropy of PolyJet elastomers is sensitive to strain rate as our reported differences in mechanical response due to anisotropy are highest at quasi-static strain rates (below 0.005 /s), and diminished at higher strain rates (above 0.3 /s) as the responses of all three orthogonal print directions converged.

In future, even higher strain rates (10 /s - 1000 /s) relevant to shock absorption and vibrational damping may be explored and may further manifest or diminish the discrepancies due to anisotropy reported here. Moreover, biaxial testing of anisotropic hyperelastic materials such as the explored 3D-printed elastomers is invaluable in providing true and complete characterisation of the mechanical properties, particularly for applications involving pressured walls such as bellow actuators.

Our findings will allow for the development of more accurate computational models of the PolyJet elastomers, which can be utilised in computer-aided designs of novel applications requiring flexible or rate-sensitive 3D-printed materials. Although PolyJet technology is fast and capable of printing multiple materials in a single build, it can also be quite expensive. This is particularly true when parts are iteratively prototyped and printed many times before a final design satisfies requirements. High-fidelity FEA on computational models can reduce printing costs and shorten time to market by reducing the number of physical iterations. One major limitation of this method is the fidelity of available AM material data, particularly of time-dependent elastomers at large strains. The material

model and properties presented here can facilitate the development of high-fidelity finite element models of A30 and T+ elastomers and provide a basis for similar developments for current and future AM elastomers.

Conclusion

In this paper, we characterise the latest and most widely employed PolyJet elastomers, A30 and T+, under a range of loading conditions and strain rates (0.003 /s - 0.5 /s) printed in different orientations relative to the print bed plane. Moreover, we present a visco-hyperelastic model that accurately captures the time-dependent response of the PolyJet materials. Our visco-hyperelastic material model was calibrated to relaxation spectra from stress relaxation and DMA tests and was able to capture the time-dependent response of both elastomers. We found the mechanical response of both elastomers to be highly nonlinear and highly dependent on strain rate and build orientation. Both elastomers had a glass transition temperature ($T_g \sim 0°C$). However, the tensile stress at 50% strain of A30 was larger than T+ and increased by 67% across two orders of magnitude of strain rate for X- and Y- samples, and by more than 127% for Z- samples. These magnitudes were smaller for T+, highlighting a lesser strain rate sensitivity. Nonetheless, a similar trend in tension was observed between build orientation and strain rates. Interestingly, anisotropy due to build orientation diminished at higher strain rates (0.3-0.5 /s). The presented visco-hyperelastic material model accurately predicted the relaxation and monotonic tension-compression responses of both PolyJet elastomers with an error between 1.3% and 16.8% for X- and Y- samples and between 4.3% and 29.9% for Z- samples depending on strain rate.

Appendices

Appendix A

Images

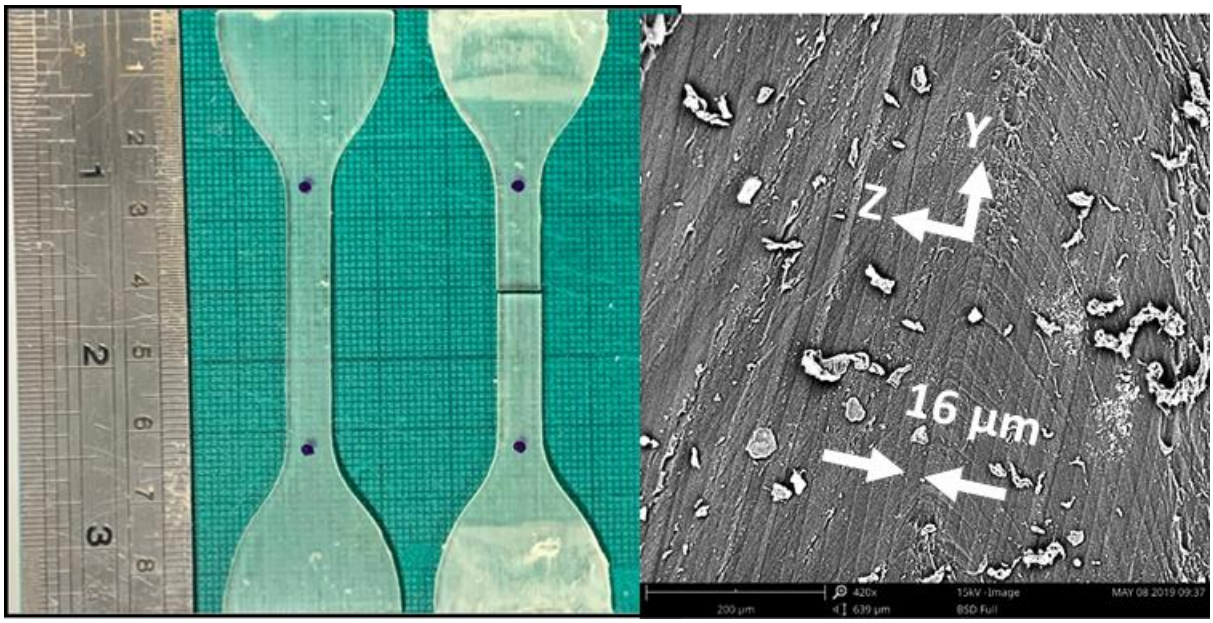


Figure 13 - comparison between pristine and failed A30 tensile specimen showing no residual plastic strain (left). Scanning electron microscope image along the Y-Z plane showing 16 micrometre layer thickness (right).

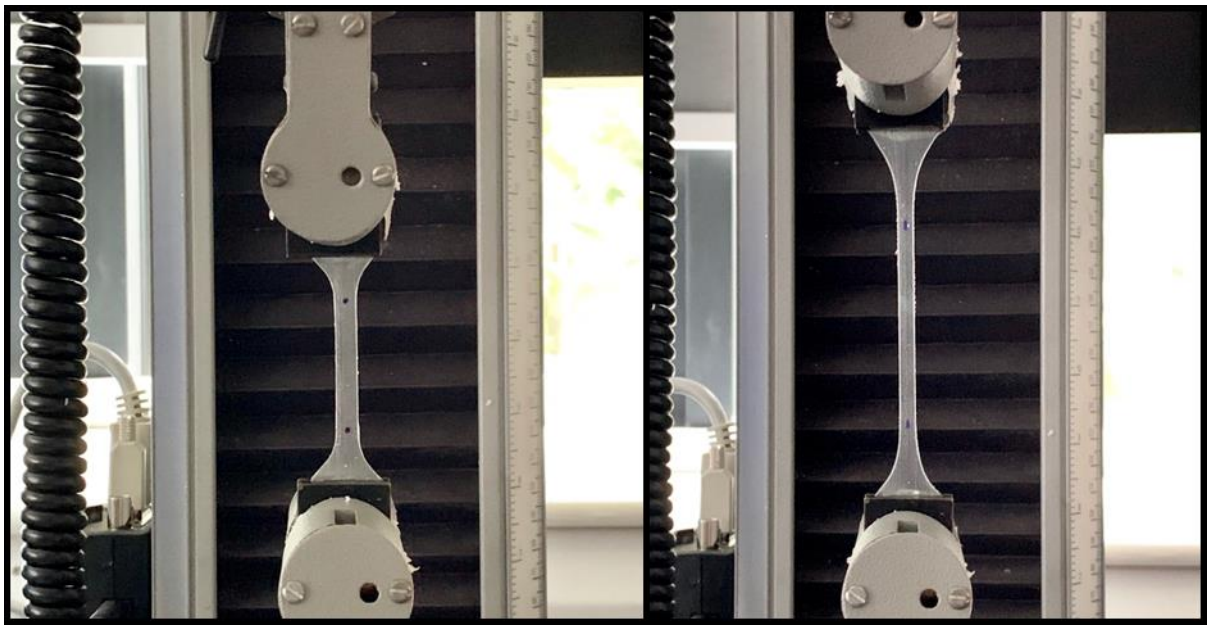


Figure 14 - A30 X- sample during tensile testing at 0.03 /s at the start of testing (left) and at 56% strain (right).

Appendix B

Tension

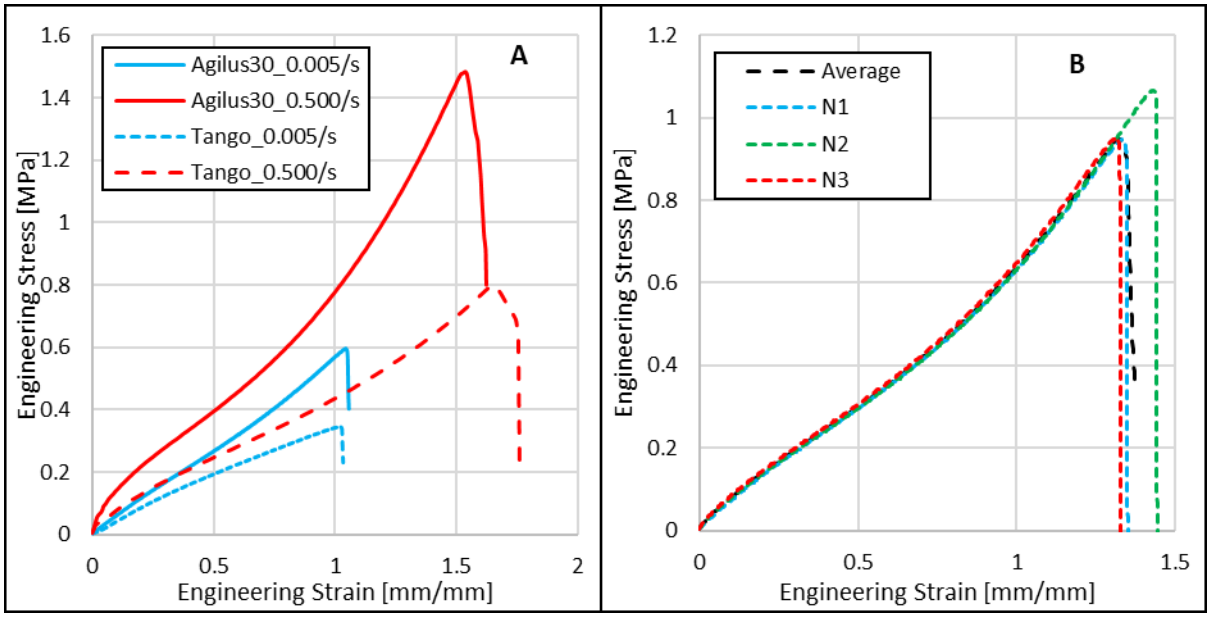


Figure 15 – (A) Comparison between A30 and Tango+ tensile responses at the lowest and highest tested strain rates and (B) exemplar set of results (A30, 0.05 /s strain rate) showing the repeatability achieved in tests.

*Table 6 - Stress values of A30 and T+ X- samples at 50% strain in compression and comparative decrease between max. and min. strain rates relative to tension. *Tension values have been reported in Table 1.*

Stress [MPa] v. Strain rate [/s] at 50% Strain	0.005 /s	0.05 /s	0.5 /s	N times larger across the two orders of magnitude of strain rate
A30				
Compression	0.787	1.161	2.179	2.77
(±SD)	0.020	0.002	0.003	
Tension	*	*	*	1.67
T+				
Compression	0.604	0.828	1.399	2.32
(±SD)	0.020	0.004	0.004	
Tension	*	*	*	1.28

Appendix C

Compression

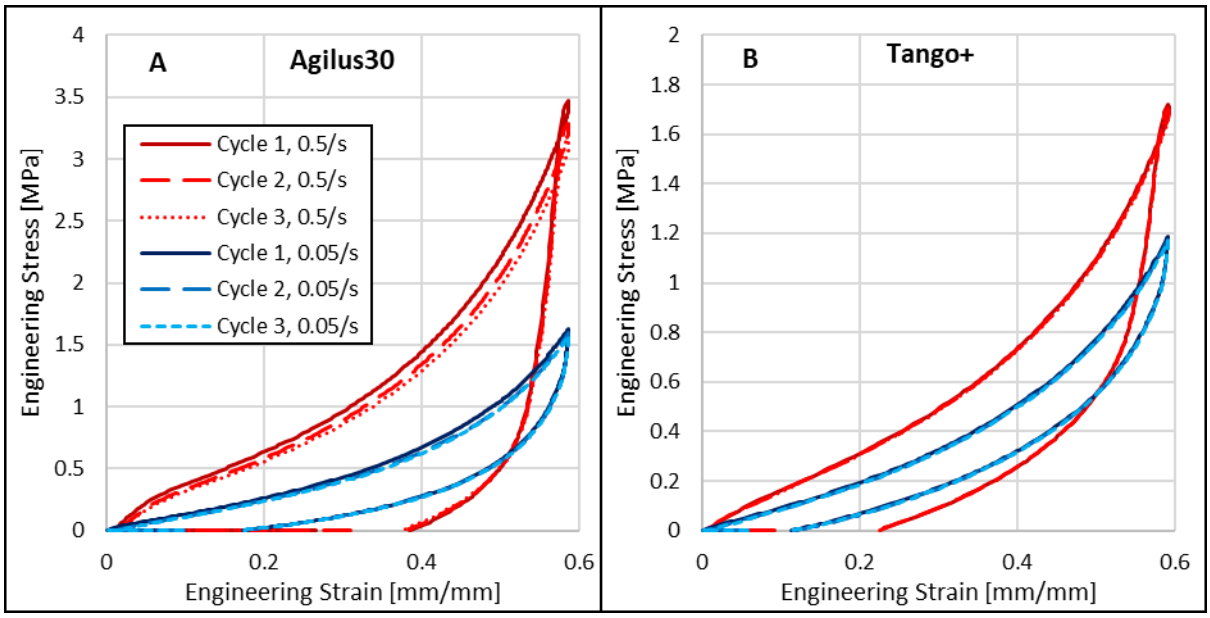


Figure 16 - Cyclic loading stress-strain curves of A30 (A) and Tango+ (B) Z- samples at a strain rate of 0.5 /s with no idling between cycles (blue) and a 20 second idle (red).

Appendix D

Stress Relaxation and DMA

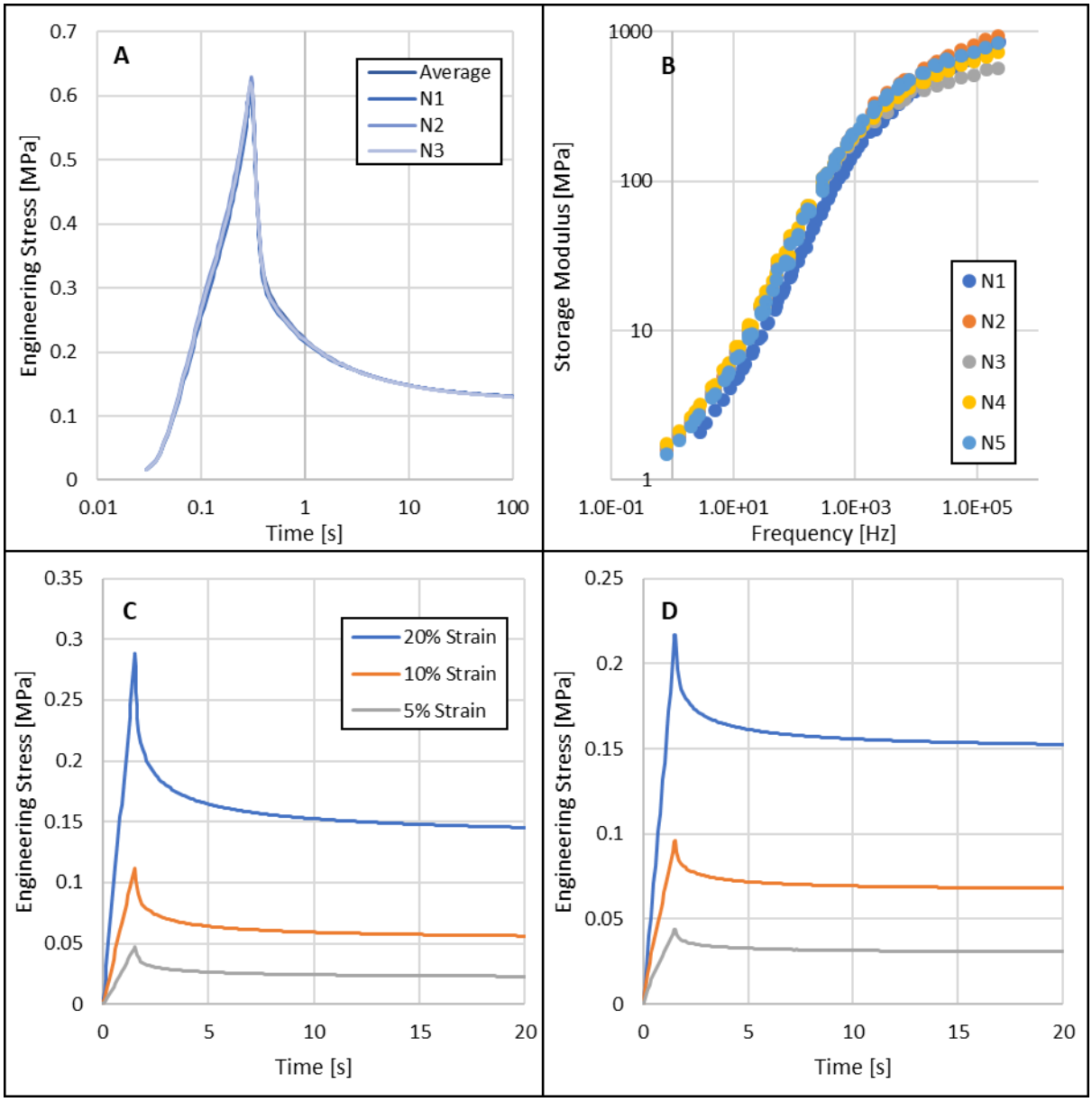


Figure 17 - Repeats of A30 relaxation tests (A) and DMA TTS results (B). Stress relaxation of A30 (C) and T+ (D) at different strain levels.

Appendix E

Determining Prony series constants from DMA results

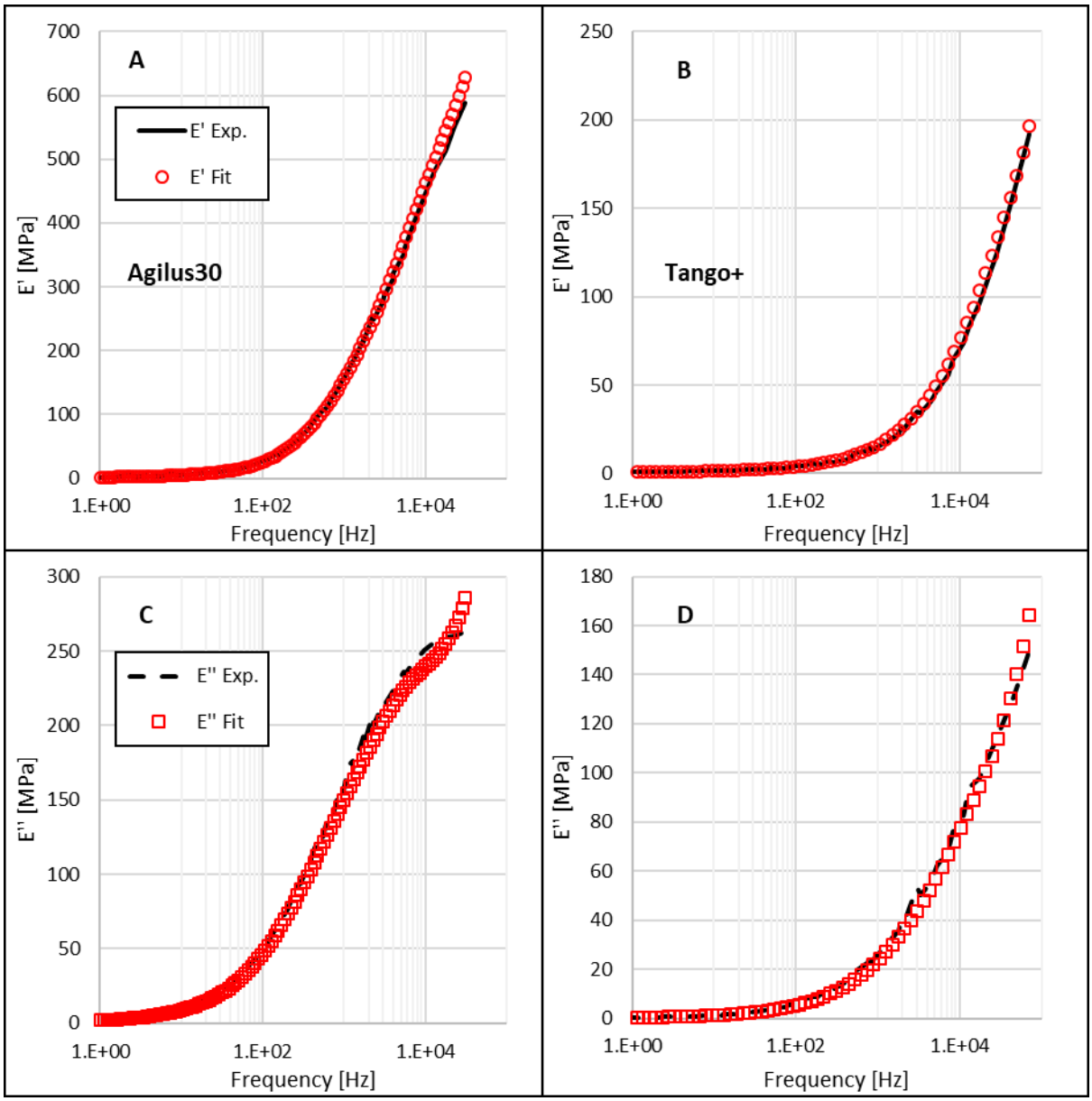


Figure 18 - Experimental vs. numerical approximation of E' and E'' master curves. The Prony series parameters obtained from this approximation were normalised by the instantaneous modulus obtained using Equation (12)-(13).

The methods to approximate the Prony series coefficients (g_i, τ_i) from relaxation spectra (E', E'') have been outlined in detail in several studies [57,64,75]. However, for the sake of completeness, the equations used for the approximation in the MATLAB code are included here.

$$E'(\omega) = E_\infty + \sum_{i=1}^{n} \frac{\tau_i^2 \omega^2 g_i}{\tau_i^2 \omega^2 + 1} \tag{12}$$

$$E''(\omega) = \sum_{i=1}^{n} \frac{\tau_i^2 \omega^2 g_i}{\tau_i^2 \omega^2 + 1} \tag{13}$$

Where:

E', E'' are storage and loss moduli respectively.

ω is the oscillatory frequency of the DMA tester.

τ_i is the ith characteristic relaxation time of the material

g_i is the ith normalised modulus of the material

The Levenberg-Marquardt method is used to obtain the fit presented in Figure 18, which resulted in 6 Prony pairs for each material spanning at least 6 orders of magnitude. As there was 1 Prony pair per time decade on average, only two Prony pairs from the DMA tests were used corresponding to 1 μs $\leq \tau \leq$ 0.1 s, as highlighted in Table 7. Pairs with larger characteristic times are more accurately predicted using relaxation tests, and smaller characteristic times were found to have no effect on the response within the window of strain rates explored here and, in any case, would increase computational effort.

Table 7 - Prony pairs for A30 and T+ obtained from DMA time-temperature superposition tests.

A30		**T+**	
g_i	**τ_i [s]**	**g_i**	**τ_i [s]**
1.11E+03	6.68E-06	7.32E+02	2.93E-06
3.29E+02	1.51E-04	1.18E+02	6.87E-05
1.68E+02	1.01E-03	2.96E+01	6.71E-04
5.69E+01	**5.08E-03**	**4.95E+00**	**9.24E-03**
8.57E+00	**4.97E-02**	**7.09E-01**	**1.73E-01**
1.88E+00	6.44E-01	8.49E-01	5.89E+00

Acknowledgements

We would like to acknowledge the Imperial College President's PhD Scholarship and the Royal Society (Research Grant no. RGS\R1\191217) for the financial support. The authors would also like to acknowledge Dr Connor Myant for his assistance with the PolyJet printing, Professor Maria Charalambides for her assistance with the numerical modelling techniques, and Dr Ruth Brooker and Mr Fabian Sorce for their assistance with their assistance with the experiments.

Conflict of Interest

The authors have no conflict of interest to declare.

References

[1] Bugatti - World premiere: brake caliper from 3-D printer, (n.d.). https://www.bugatti.com/media/news/2018/world-premiere-brake-caliper-from-3-d-printer/ (accessed August 7, 2019).

[2] Y.C. Wang, T. Chen, Y.L. Yeh, Advanced 3D printing technologies for the aircraft industry: a fuzzy systematic approach for assessing the critical factors, Int. J. Adv. Manuf. Technol. (2018) 1–11. https://doi.org/10.1007/s00170-018-1927-8.

[3] A.D. Knight, P.P. Anderson, M.D. Beachler, C.L. Dearth, L.M. Hassinger, B.D. Hendershot, T.J. Sleeman, P.C. Liacouras, Customized 3D-Printed Prosthetic Devices for Wounded Warriors, Am. J. Phys. Med. Rehabil. 98 (2018) 1. https://doi.org/10.1097/phm.0000000000001047.

[4] D. Ackland, D. Robinson, P.V.S. Lee, G. Dimitroulis, Design and clinical outcome of a novel 3D-printed prosthetic joint replacement for the human temporomandibular joint, Clin. Biomech. 56 (2018) 52–60. https://doi.org/10.1016/j.clinbiomech.2018.05.006.

[5] B. Rochlitz, D. Pammer, R. Kiss, Functionality and load-bearing analysis of 3D-printed prosthetic feet, Mater. Today Proc. 5 (2018) 26566–26571. https://doi.org/10.1016/j.matpr.2018.08.117.

[6] X. Li, Y. Wang, Y. Zhao, J. Liu, S. Xiao, K. Mao, Multilevel 3D Printing Implant for Reconstructing Cervical Spine with Metastatic Papillary Thyroid Carcinoma, Spine (Phila. Pa. 1976). 42 (2017) E1326–E1330. https://doi.org/10.1097/BRS.0000000000002229.

[7] S.F. Khosroshahi, S.A. Tsampas, U. Galvanetto, Feasibility study on the use of a hierarchical lattice architecture for helmet liners, Mater. Today Commun. 14 (2018) 312–323. https://doi.org/10.1016/j.mtcomm.2018.02.002.

[8] S.F. Khosroshahi, H. Duckworth, U. Galvanetto, M. Ghajari, The effects of topology and relative density of lattice liners on traumatic brain injury mitigation, J. Biomech. 97 (2019) 109376. https://doi.org/10.1016/j.jbiomech.2019.109376.

[9] A.J. Jacobsen, W. Barvosa-Carter, S. Nutt, Micro-scale truss structures formed from self-propagating photopolymer waveguides, Adv. Mater. 19 (2007) 3892–3896. https://doi.org/10.1002/adma.200700797.

[10] C. Qiu, S. Yue, N.J.E. Adkins, M. Ward, H. Hassanin, P.D. Lee, P.J. Withers, M.M. Attallah, Influence of processing conditions on strut structure and compressive properties of cellular lattice structures fabricated by selective laser melting, Mater. Sci. Eng. A. 628 (2015) 188–197. https://doi.org/10.1016/j.msea.2015.01.031.

[11] Z. Ozdemir, A. Tyas, R. Goodall, H. Askes, Energy absorption in lattice structures in dynamics: Nonlinear FE simulations, Int. J. Impact Eng. 102 (2017) 1–15. https://doi.org/10.1016/j.ijimpeng.2016.11.016.

[12] N.A. Meisel, D.A. Dillard, C.B. Williams, Impact of material concentration and distribution on composite parts manufactured via multi-material jetting, Rapid Prototyp. J. 24 (2018) 872–879. https://doi.org/10.1108/RPJ-01-2017-0005.

[13] J. Herzberger, J.M. Sirrine, C.B. Williams, T.E. Long, Polymer Design for 3D Printing Elastomers: Recent Advances in Structure, Properties, and Printing, Prog. Polym. Sci. 97 (2019) 101144. https://doi.org/10.1016/j.progpolymsci.2019.101144.

[14] S. Akbari, A.H. Sakhaei, K. Kowsari, B. Yang, A. Serjouei, Z. Yuanfang, Q. Ge, Enhanced multimaterial 4D printing with active hinges, Smart Mater. Struct. 27 (2018). https://doi.org/10.1088/1361-665X/aabe63.

[15] K. Che, C. Yuan, H.J. Qi, J. Meaud, Viscoelastic multistable architected materials with temperature-dependent snapping sequence, Soft Matter. 14 (2018) 2492–2499. https://doi.org/10.1039/c8sm00217g.

[16] Q. Ge, G. Gu, D. Wang, B. Zhang, N. Zhang, C. Yuan, H. Hingorani, N. Ding, Y.-F. Zhang, Fast-Response, Stiffness-Tunable Soft Actuator by Hybrid Multimaterial 3D Printing, Adv. Funct. Mater. (2019) 1806698. https://doi.org/10.1002/adfm.201806698.

[17] G. Dammer, S. Gablenz, A. Hildebrandt, Z. Major, Design and shape optimization of PolyJet bellows actuators, 2018 IEEE Int. Conf. Soft Robot. RoboSoft 2018. (2018) 282–287. https://doi.org/10.1109/ROBOSOFT.2018.8404933.

[18] A. Kakogawa, S. Ma, A Differential Elastic Joint for Multi-linked Pipeline Inspection Robots, IEEE Int. Conf. Intell. Robot. Syst. (2018) 949–954. https://doi.org/10.1109/IROS.2018.8593872.

[19] Z. Ding, C. Yuan, X. Peng, T. Wang, H.J. Qi, M.L. Dunn, Direct 4D printing via active composite materials, Sci. Adv. 3 (2017). https://doi.org/10.1126/sciadv.1602890.

[20] T. Chen, O.R. Bilal, K. Shea, C. Daraio, Harnessing bistability for directional propulsion of untethered, soft robots, (2017). https://doi.org/10.1073/pnas.1800386115.

[21] Y. Mao, Z. Ding, C. Yuan, S. Ai, M. Isakov, J. Wu, T. Wang, M.L. Dunn, H.J. Qi, 3D Printed Reversible Shape Changing Components with Stimuli Responsive Materials., Sci. Rep. 6 (2016) 24761. https://doi.org/10.1038/srep24761.

[22] S.N.R. Kantareddy, T.W. Simpson, Z. Ounaies, M. Frecker, 3D Printing of Shape Changing Polymer Structures: Design and Characterization of Materials, Solid Free. Fabr. Symp. (2016) 2224–2235. http://sffsymposium.engr.utexas.edu/sites/default/files/2016/178-Kantareddy.pdf.

[23] J. Wu, C. Yuan, Z. Ding, M. Isakov, Y. Mao, T. Wang, M.L. Dunn, H.J. Qi, Multi-shape active composites by 3D printing of digital shape memory polymers, Sci. Rep. 6 (2016) 1–11. https://doi.org/10.1038/srep24224.

[24] L.S. Dimas, G.H. Bratzel, I. Eylon, M.J. Buehler, Tough composites inspired by mineralized natural materials: Computation, 3D printing, and testing, Adv. Funct. Mater. 23 (2013) 4629–4638. https://doi.org/10.1002/adfm.201300215.

[25] Y. Han, W.F. Lu, Structural design of wearable electronics suitable for highly-stretched joint areas, Smart Mater. Struct. 27 (2018). https://doi.org/10.1088/1361-665X/aadf05.

[26] D.M.J. Dykstra, J. Busink, B. Ennis, C. Coulais, Viscoelastic Metamaterials, (2019). http://arxiv.org/abs/1904.11888.

[27] V. Slesarenko, S. Rudykh, Towards mechanical characterization of soft digital materials for multimaterial 3D-printing, Int. J. Eng. Sci. 123 (2018) 62–72. https://doi.org/10.1016/j.ijengsci.2017.11.011.

[28] V. Slesarenko, S. Rudykh, Harnessing viscoelasticity and instabilities for tuning wavy patterns in soft layered composites, Soft Matter. 12 (2016) 3677–3682. https://doi.org/10.1039/c5sm02949j.

[29] S. Rudykh, C. Ortiz, M.C. Boyce, Flexibility and protection by design: Imbricated hybrid microstructures of bio-inspired armor, Soft Matter. 11 (2015) 2547–2554. https://doi.org/10.1039/c4sm02907k.

[30] H. Cho, J.C. Weaver, E. Pöselt, P.J. in't Veld, M.C. Boyce, G.C. Rutledge, Engineering the Mechanics of Heterogeneous Soft Crystals, Adv. Funct. Mater. 26 (2016) 6938–6949. https://doi.org/10.1002/adfm.201601719.

[31] A.S. Dalaq, D.W. Abueidda, R.K. Abu Al-Rub, I.M. Jasiuk, Finite element prediction of effective elastic properties of interpenetrating phase composites with architectured 3D sheet reinforcements, Int. J. Solids Struct. 83 (2016) 169–182. https://doi.org/10.1016/j.ijsolstr.2016.01.011.

[32] V. Slesarenko, N. Kazarinov, S. Rudykh, Distinct failure modes in bio-inspired 3D-printed staggered composites under non-aligned loadings, Smart Mater. Struct. 26 (2017). https://doi.org/10.1088/1361-665X/aa59eb.

[33] J. Shen, S. Zhou, X. Huang, Y.M. Xie, Simple cubic three-dimensional auxetic metamaterials, Phys. Status Solidi Basic Res. 251 (2014) 1515–1522. https://doi.org/10.1002/pssb.201451304.

[34] A.S. Dalaq, D.W. Abueidda, R.K. Abu Al-Rub, Mechanical properties of 3D printed interpenetrating phase composites with novel architectured 3D solid-sheet reinforcements, Compos. Part A Appl. Sci. Manuf. 84 (2016) 266–280. https://doi.org/10.1016/j.compositesa.2016.02.009.

[35] L. Wang, J. Lau, E.L. Thomas, M.C. Boyce, Co-continuous composite materials for stiffness, strength, and energy dissipation, Adv. Mater. 23 (2011) 1524–1529. https://doi.org/10.1002/adma.201003956.

[36] L. Bass, N.A. Meisel, C.B. Williams, Exploring variability of orientation and aging effects in material properties of multi-material jetting parts, Rapid Prototyp. J. 22 (2016) 826–834. https://doi.org/10.1108/RPJ-11-2015-0169.

[37] J.E. Ryu, E. Salcedo, H.J. Lee, S.J. Jang, E.Y. Jang, H. Al Yassi, D. Baek, D. Choi, E. Lee, Material models and finite analysis of additively printed polymer composites, (2019). https://doi.org/10.1177/0021998318785672.

[38] E. Salcedo, D. Baek, A. Berndt, J.E. Ryu, Simulation and validation of three dimension functionally graded materials by material jetting, Addit. Manuf. 22 (2018) 351–359. https://doi.org/10.1016/j.addma.2018.05.027.

[39] G. Dämmer, S. Gablenz, A. Hildebrandt, Z. Major, PolyJet-printed bellows actuators: Design, structural optimization, and experimental investigation, Front. Robot. AI. 6 (2019) 1–10. https://doi.org/10.3389/frobt.2019.00034.

[40] A. KĘSY, J. KOTLIŃSKI, Mechanical properties of parts produced by using polymer jetting technology, Arch. Civ. Mech. Eng. 10 (2012) 37–50. https://doi.org/10.1016/s1644-9665(12)60135-6.

[41] T. Stanković, J. Mueller, K. Shea, The effect of anisotropy on the optimization of additively manufactured lattice structures, Addit. Manuf. 17 (2017) 67–76. https://doi.org/10.1016/j.addma.2017.07.004.

[42] J. Mueller, K. Shea, C. Daraio, Mechanical properties of parts fabricated with inkjet 3D printing through efficient experimental design, Mater. Des. 86 (2015) 902–912. https://doi.org/10.1016/j.matdes.2015.07.129.

[43] A. Cazón, P. Morer, L. Matey, PolyJet technology for product prototyping: Tensile strength and surface roughness properties, Proc. Inst. Mech. Eng. Part B J. Eng. Manuf. 228 (2014) 1664–1675. https://doi.org/10.1177/0954405413518515.

[44] D. Blanco, P. Fernandez, A. Noriega, Nonisotropic experimental characterization of the relaxation modulus for PolyJet manufactured parts, J. Mater. Res. 29 (2014) 1876–1882. https://doi.org/10.1557/jmr.2014.200.

[45] H. Miyanaji, N. Momenzadeh, L. Yang, Effect of printing speed on quality of printed parts in Binder Jetting Process, Addit. Manuf. 20 (2018) 1–10. https://doi.org/10.1016/j.addma.2017.12.008.

[46] G. Yerbolat, A. Shynggys, M.H. Ali, Mechanical property prediction method based on multi-material 3D printer, 2018 Jt. 7th Int. Conf. Informatics, Electron. Vis. 2nd Int. Conf. Imaging, Vis. Pattern Recognition, ICIEV-IVPR 2018. (2019) 498–502. https://doi.org/10.1109/ICIEV.2018.8641073.

[47] V.S. Joshi, C. Qualters, E. Chen, J.R. Santiago, K. O'Neill, Dynamic characterization of anisotropy effects in 3-D printed materials for high-G survivability, AIP Conf. Proc. 1979 (2018). https://doi.org/10.1063/1.5044924.

[48] R. Adams, S.P. Soe, R. Santiago, M. Robinson, B. Hanna, G. McShane, M. Alves, R. Burek, P. Theobald, A novel pathway for efficient characterisation of additively manufactured thermoplastic elastomers, Mater. Des. 180 (2019) 107917. https://doi.org/10.1016/j.matdes.2019.107917.

[49] I.Q. Vu, L.B. Bass, C.B. Williams, D.A. Dillard, Characterizing the effect of print orientation on interface integrity of multi-material jetting additive manufacturing, Addit. Manuf. 22 (2018) 447–461. https://doi.org/10.1016/j.addma.2018.05.036.

[50] B. Standards, BS ISO 37 : 2017 BSI Standards Publication Rubber , vulcanized or thermoplastic — Determination of tensile stress-strain properties, (2017).

[51] B. Standards, BS ISO 7743 : 2017 BSI Standards Publication Rubber , vulcanized or thermoplastic — Determination of compression stress-strain properties, (2017).

[52] TA Instruments, TA Instruments DMA Q800 Specifications, (2010) 1–14.

[53] D. Gutierrez-Lemini, Engineering viscoelasticity, Eng. Viscoelasticity. (2014) 1–353. https://doi.org/10.1007/978-1-4614-8139-3.

[54] G.W. Ehrenstein, G. Riedel, P. Trawiel, Chapter 6 Dynamic Mechanical Analysis, Therm. Anal. Plast. Theory Pract. (2004) 236–299.

[55] S.H. Chae, J.H. Zhao, D.R. Edwards, P.S. Ho, Characterization of the Viscoelasticity of Molding Compounds in the Time Domain, J. Electron. Mater. 39 (2010) 419–425. https://doi.org/10.1007/s11664-010-1078-7.

[56] R.W. Ogden, G. Saccomandi, I. Sgura, Fitting hyperelastic models to experimental data, Comput. Mech. 34 (2004) 484–502. https://doi.org/10.1007/s00466-004-0593-y.

[57] Dassault Systèmes Simulia, Analysis User's Manual Volume 3: Materials, Abaqus 6.12. III (2012).

[58] T. Frank, A. Kurz, M. Pitzer, M. Söllner, Development and validation of numerical pedestrian impactor models, 4th Eur. LS-DYNA Users Conf. (2003) 1–18.

[59] C.M. Roland, Viscoelastic Behavior of Rubbery Materials, Viscoelastic Behav. Rubbery Mater. 9780199571 (2011) 1–344. https://doi.org/10.1093/acprof:oso/9780199571574.001.0001.

[60] G.A. Holzapfel, Nonlinear Solid Mechanics : a Continuum Approach for Engineering, Work. First Edit (2000) 205. https://doi.org/10.1023/A:1020843529530.

[61] H. Cho, S. Mayer, E. Pöselt, M. Susoff, P.J. Veld, G.C. Rutledge, M.C. Boyce, Deformation mechanisms of thermoplastic elastomers: Stress-strain behavior and constitutive modeling, Polymer (Guildf). 128 (2017) 87–99. https://doi.org/10.1016/j.polymer.2017.08.065.

[62] C. Tzikang, Determining a Prony Series for a Viscoelastic Material From Time Varying Strain Data, Nasa. (2000).

[63] S.M. Goh, M.N. Charalambides, J.G. Williams, Determination of the constitutive constants of non-linear viscoelastic materials, Mech. Time-Dependent Mater. 8 (2004) 255–268. https://doi.org/10.1023/B:MTDM.0000046750.65395.fe.

[64] A. Takeh, S. Shanbhag, A computer program to extract the continuous and discrete relaxation spectra from dynamic viscoelastic measurements, Appl. Rheol. 23 (2013) 1–10. https://doi.org/10.3933/ApplRheol-23-24628.

[65] R.L. Taylor, K.S. Pister, G.L. Goudreau, Thermomechanical analysis of viscoelastic solids, Int. J. Numer. Methods Eng. 2 (1970) 45–59.

[66] M. Kaliske, H. Rothert, Formulation and implementation of three-dimensional viscoelasticity at small and finite strains, Comput. Mech. 19 (1997) 228–239. https://doi.org/10.1007/s004660050171.

[67] H. Cho, R.G. Rinaldi, M.C. Boyce, Constitutive modeling of the rate-dependent resilient and dissipative large deformation behavior of a segmented copolymer polyurea, Soft Matter. 9 (2013) 6319–6330. https://doi.org/10.1039/c3sm27125k.

[68] R.G. Rinaldi, M.C. Boyce, S.J. Weigand, D.J. Londono, M.W. Guise, Microstructure evolution during tensile loading histories of a polyurea, J. Polym. Sci. Part B Polym. Phys. 49 (2011) 1660–1671. https://doi.org/10.1002/polb.22352.

[69] D. Mohotti, T. Ngo, S.N. Raman, M. Ali, P. Mendis, Plastic deformation of polyurea coated composite aluminium plates subjected to low velocity impact, Mater. Des. 56 (2014) 696–713. https://doi.org/10.1016/j.matdes.2013.11.063.

[70] D. Mohotti, T. Ngo, P. Mendis, S.N. Raman, Polyurea coated composite aluminium plates subjected to high velocity projectile impact, Mater. Des. 52 (2013) 1–16. https://doi.org/10.1016/j.matdes.2013.05.060.

[71] R.D. Hussein, D. Ruan, G. Lu, S. Guillow, J.W. Yoon, Crushing response of square aluminium tubes filled with polyurethane foam and aluminium honeycomb, Thin-Walled Struct. 110 (2017) 140–154. https://doi.org/10.1016/j.tws.2016.10.023.

[72] S.S. Sarva, S. Deschanel, M.C. Boyce, W. Chen, Stress-strain behavior of a polyurea and a polyurethane from low to high strain rates, Polymer (Guildf). 48 (2007) 2208–2213. https://doi.org/10.1016/j.polymer.2007.02.058.

[73] M.H.R. Ghoreishy, Determination of the parameters of the Prony series in hyper-viscoelastic material models using the finite element method, Mater. Des. 35 (2012) 791–797. https://doi.org/10.1016/j.matdes.2011.05.057.

[74] M.A.P. Mohammed, E. Tarleton, M.N. Charalambides, J.G. Williams, Mechanical characterization and micromechanical modeling of bread dough, J. Rheol. (N. Y. N. Y). 57 (2012) 249–272. https://doi.org/10.1122/1.4768463.

[75] I. Emri, B.S. von Bernstorff, R. Cvelbar, A. Nikonov, Re-examination of the approximate methods for interconversion between frequency- and time-dependent material functions, J. Nonnewton. Fluid Mech. 129 (2005) 75–84. https://doi.org/10.1016/j.jnnfm.2005.05.008.